catalysts

MDPI

Review

Co_3O_4 Catalysts for Complete Toluene Oxidation: Review including Meta-Analysis of Catalyst Activity Data

Yiannis Georgiou, Maria Smyrnioti and Theophilos Ioannides *

Foundation for Research and Technology-Hellas, Institute of Chemical Engineering Sciences (FORTH/ICE-HT), GR-26504 Patras, Greece; msmyrnioti@iceht.forth.gr (M.S.)
* Correspondence: theo@iceht.forth.gr

Abstract: Designing highly active catalysts for the oxidation of volatile organic compounds (VOCs) involves fine-tuning the catalytic surface and improving its interaction with VOCs. The present review assesses various studies conducted in the last decade on Co_3O_4 catalysts for the complete oxidation of toluene (C_7H_8) and provides information on the synthesis and physicochemical characterization of these catalysts. Taking this one step further, data from the literature were carefully chosen for an extensive meta-analysis aiming at elucidating the structure sensitivity of toluene oxidation over Co_3O_4 catalysts. Specifically, the specific reaction rate was calculated and correlated with the physicochemical properties of the catalysts, namely, the specific surface area, faceting, and Co^{3+}/Co^{2+} ratio. Based on this analysis, the specific surface area does not exert a significant impact on the specific activity of Co_3O_4 catalysts for the total oxidation of toluene. Instead, the specific reaction rates are influenced by the morphology, surface concentration, exposed crystallographic planes, and oxidation state of cobalt cations. These factors determine the catalyst's specific activity by creating defects, oxygen vacancies, or oxygen species with different reactivities. It was also found that a high surface Co^{3+}/Co^{2+} ratio is necessary for achieving high catalytic performance in the oxidation of VOCs.

Keywords: cobalt oxide catalysts; complete oxidation; toluene; structure sensitivity

check for updates

Citation: Georgiou, Y.; Smyrnioti, M.; Ioannides, T. Co_3O_4 Catalysts for Complete Toluene Oxidation: Review including Meta-Analysis of Catalyst Activity Data. *Catalysts* **2023**, *13*, 1454. https://doi.org/10.3390/catal13111454

Academic Editor: Stefano Cimino

Received: 4 November 2023
Revised: 15 November 2023
Accepted: 16 November 2023
Published: 20 November 2023

1. Introduction

The emission of volatile organic compounds (VOCs) has been found to have detrimental effects on both human health and the environment. The emission source determines the type and composition of the VOCs. Examples of VOCs include halogenated hydrocarbons, alcohols, aldehydes, aromatics, alkanes, ketones, olefins, ethers, esters, and sulfur-containing compounds [1–3].

These molecules are dispersed in the atmosphere and can travel over vast expanses [4]. There are multiple outdoor and indoor sources of VOCs [5,6]. Outdoor sources [6–8] include, but are not limited to, chemical industries, paper production, food processing, paint drying, transportation, petroleum refineries, automobile manufacturing, metal degreasing, textile manufacturing, electronic component plants, solvents, and cleaning products. Indoor sources [9] include household products, office supplies, printers, heat exchanger systems, insulating materials, pressed wood, wood stoves, and pipe leaks. Exposure to VOCs can cause various adverse health effects, including irritation, asthma exacerbation, allergy, respiratory effects, and cancer [10].

Aftertreatment technologies for VOC emission control can be classified into two categories based on the recovery or destruction of the pollutant. Methods for the recovery of VOCs include condensation, absorption, adsorption, and membrane separation. VOC destruction involves incineration methods, focusing on thermal [11] and catalytic oxidation [12,13], where the non-halogenated VOC is converted to carbon dioxide and water. When air is used as an oxidant in thermal oxidation, nitrogen oxides (NO_x) and dioxins are also produced as by-products. In contrast, catalytic oxidation is more effective and environmentally friendly

as it takes place at lower temperatures with minor by-product formation. Operating at low temperatures is necessary to reduce energy consumption and operating costs. However, thermal incineration excels at high VOC concentrations and flow rates.

Precious metals are among the most active catalysts for the oxidation of VOCs [14,15]. Pt and Pd are the most common examples, mainly supported on carriers with high surface areas, such as alumina [16]. However, the high cost and scarcity of noble metals are limiting factors that raise sustainability concerns. Consequently, attention has been also paid to transition metal oxide (TMOs) catalysts for complete VOC oxidation [17–19]. Although TMOs typically have lower activity compared to noble metal catalysts, they are less prone to poisoning. Supported and unsupported oxides include single- or mixed-metal oxides containing two or more transition metal elements [20]. The present study refers to simple transition metal oxides and, more specifically, Co_3O_4. The selection of a single oxide has been made in order to exclude the influence of interactions among various phases or the support, which complicates the analysis of catalytic performance metrics. The most studied single-metal oxides for the total oxidation of VOCs are Co_3O_4 [21–24], Mn_2O_3 [25–27], Fe_2O_3 [28], CuO [29,30], and CeO_2 [31,32]. Co_3O_4 has been widely studied because of its high activity and stability for the complete oxidation of VOCs [32,33].

The most stable phase among CoO, Co_2O_3, and Co_3O_4 is Co_3O_4 [34]. Co_3O_4 is an oxide with a typical spinel crystal structure and is a mixed-valence oxide of CoO and Co_2O_3 [35]. Co^{2+} and Co^{3+} occupy the tetrahedral and octahedral cation sites, respectively [36]. The oxidation of VOCs over Co_3O_4 involves the adsorption of organic compounds at anionic oxygen sites in the oxide lattice, leading to the formation of an activated complex. This complex further reacts to yield oxidation products. The total oxidation of toluene proceeds via C-H bond activation, followed by the formation of benzyl species and the release of hydrogen. Active oxygen species react with the benzyl species to form benzyl alcohol, which is further oxidized to a series of products, including benzaldehyde, benzoic acid, benzene, phenol, benzoquinone, maleic anhydride, various ring-opened byproducts, and finally, carbon dioxide and water [37,38]. Lattice oxygen participates in the catalytic cycle and is regenerated by the supply of gas–phase oxygen adsorbed on a surface oxygen vacancy. Redox models can be used to describe the oxidation of VOCs on reducible metal oxides. This model can be described simply as a reduction of the surface by molecules of volatile organic compounds and the reoxidation of the catalytic surface by gaseous oxygen (Equations (1) and (2)). Scheme 1 is commonly known as the Mars–van Krevelen (MvK) mechanism [39] and is given below.

$$\textit{Surface Reduction: } VOC + \{Ox\} \rightarrow \{Red\} + \textit{oxidation products} \quad (1)$$

$$\textit{Surface Re-oxidation: } \{Red\} + O_2 \rightarrow \{Ox\} \quad (2)$$

where *{Ox}* is an oxidized surface site (e.g., lattice oxygen) and *{Red}* is a reduced surface site.

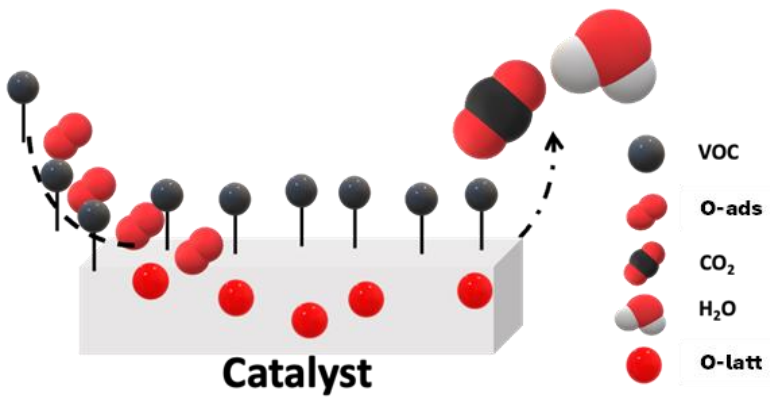

Scheme 1. MvK reaction mechanism.

The corresponding MvK rate expression for the oxidation of the VOC, r, is given by Equation (3).

$$r = \frac{k_r\, k_{ox}\, p_{VOC}\, p_{O2}}{\gamma\, k_r\, p_{VOC} + k_{ox}\, p_{O2}} \tag{3}$$

with

k_r, the surface reduction rate constant;
k_{ox}, the surface reoxidation rate constant;
p_{VOC}, the partial pressure of the VOC;
p_{O_2}, the partial pressure of oxygen;
γ, the stoichiometric coefficient for the total oxidation.

According to Vannice [40], the MvK kinetic model for oxidation reactions on solid catalysts, as originally stated, is inconsistent and incorrect. Consequently, the rate expression derived from this model is inapplicable except for one particular situation that involves the adsorption of O_2 molecules on a single site. However, this model is still inconsistent because O ions (or atoms) are proposed as reactive oxygen species rather than adsorbed O_2 molecules. Consequently, the form of the rate expression in Equation (3) has no physical relevance and must be viewed only as a mathematical fitting function. Carreto et al. [41] agreed with the hypothesis proposed by Vannice [40] and stated that a conceptual shortfall of the original meaning of the "MvK mechanism" is that in a (sub) monolayer catalyst, it is hard to identify a "lattice" oxygen species, as such a catalyst has only surface atoms. Therefore, it would be most helpful to avoid the term MvK and state specifically the structural properties (oxygen abundance, oxidation state, binding energy of oxygen, oxygen species). Thus, the MvK equation is inaccurate because it does not specify the structural properties. Hence, kinetic exchange experiments using isotopes are required. However, the chemical potential that controls the kinetics of oxygen exchange has rarely been considered. Furthermore, the fact that oxides can exchange oxygen species does not imply that their catalytic functions are based on these properties.

Most surface studies have focused on the structural effects of metal oxides and surface reactivity [42]. According to Barteau and Vohs [43], the catalytic reaction rate depends on the geometric structure of the surface atoms on which it occurs, which is implicit in catalysis. These concepts are most commonly used for transition-metal-catalyzed reactions. In this case, structural sensitivity is almost always correlated with specificity [44]. Many authors have investigated the sensitivity of the structure of Pt [45,46], Rh [47], Pd [46], and Au [48], while few studies have focused on metal oxides [49] or mixed-metal oxides [50].

On the other hand, one of the first metal oxides selected to investigate structural sensitivity was MoO_3 [49,51]. The crystallite size of the catalyst can influence the specific catalytic activity, according to Boudart in 1969 [44], whose research work proposes that the catalytic behavior of the considered materials is optimized by tuning the morphology of the particles or bulk structures, and therefore, the specific surface area (S_{BET}) of the material. In general, the oxidizing power of a metal oxide surface can be associated with the strength of the metal–oxygen bond and the possibility of incorporating molecular oxygen into the crystal lattice, that is, the ability to re-oxidize the reduced active sites with gaseous oxygen. On the contrary, the absence of weakly bonded oxygen species may be fundamental in determining the reaction path and catalyst selectivity.

Interestingly, the influence of the acidic and basic properties of the surface should also be considered [52]. The simplest way to change the surface structure of a metal crystallite is to alter its particle size (which is related to the specific surface area). The other is by employing different synthesis methods to change the crystal shape and morphology. The structure sensitivity demonstrates how different surface structures can lead to reactions or activation within the same molecule. When such materials are designed, the activity and selectivity of the catalysts can be controlled by carefully manipulating the surface and bulk structure of the formulated particles.

Regarding the preparation of Co_3O_4 catalysts, a multitude of synthesis methods have been employed, including hydrothermal, solvothermal [53], sol–gel [54], thermal

decomposition [24], chemical precipitation, and hard or soft templates [55]. Different synthesis methods can produce various morphologies and structures, such as nanowires [56], nanoboxes [57], nanoparticles [58], nanorods [59], nanoflowers [32], and nanobrushes [60]. The above studies were triggered by the fact that Co_3O_4 is a versatile oxide whose properties can be used in applications such as solid-state sensors [59,61], lithium-ion batteries [62], and medicine [63]. Although several review articles have been published on the complete catalytic oxidation of VOCs by Co_3O_4 [64] or other transition metal oxides [65–67], only one review article has focused on the structural activity with respect to the exposed planes of Co_3O_4 [42]. That study focused on the total oxidation of carbon monoxide.

For this purpose, the current review has been structured to shed light on the following question: "Is the specific reaction rate of VOC oxidation over Co_3O_4 dependent on its specific surface area or its crystallite size and at a second level, does it depend on its exposed crystallographic planes induced by the different morphology?" In other words, is VOC oxidation over Co_3O_4 a structure-sensitive reaction? To answer these questions, the oxidation of toluene serves as a case study. Additionally, this work presents and analyzes the main physicochemical characterization, the various synthesis methods in relation to the obtained morphologies, and the effect of the specific surface area of Co_3O_4 catalysts.

2. Evaluating the Surface Activity of Co_3O_4 Catalysts for Complete Toluene Oxidation

2.1. General Information on the Experimental Procedure for Complete Toluene Oxidation

In most of the research articles examined in this review, complete toluene oxidation was performed in fixed-bed tubular reactors. The reaction rate of VOC oxidation was calculated using Equation (4), where r_{VOC} is the reaction rate of VOC oxidation (mol s^{-1} g_{cat}^{-1}), F is the total flow rate (mol s^{-1}), W is the mass of the catalyst (g), and C_{VOC}^{in} and C_{VOC}^{out} are the inlet and outlet molar fractions of the VOC, respectively. Dividing the reaction rate by the specific surface area produces the specific reaction rate (SRR), r_{srr}(mol s^{-1} m_{cat}^{-2}).

$$r_{VOC} = \frac{(C_{VOC}^{in} - C_{VOC}^{out})F}{W} \quad (4)$$

It should be mentioned that if the reaction rate was not reported in the examined research articles, it was calculated by extracting the experimental data from the light-off curves (conversion vs. reaction temperature plots) presented. The conversion should typically be less than 20%, and the data are presented as the specific reaction rate (SRR) vs. 1000/T (K^{-1}) vs. temperature (°C). In addition, in the absence of experimental data for the same temperatures for all catalysts, the points were extended along a straight line to make a relevant comparison. The toluene concentration in the reactor feed was in the range of 500–1000 ppm, while the O_2 concentration varied between 10 and 20% in all research articles.

The main intention of this review article is to examine whether the specific reaction rate of VOC oxidation over Co_3O_4 depends on the following factors:

- the specific surface area of Co_3O_4 or, equivalently, the crystallite size of Co_3O_4,
- the morphology and, therefore, the exposed crystallographic planes of Co_3O_4.
- the molar Co^{3+}/Co^{2+} ratio derived mainly from XPS and H_2-TPR analyses.

This section investigates the specific activity of the catalyst related to its specific surface area vs. dominant exposed crystallographic planes obtained by various preparation methods. It is also been determined whether the specific activity can be correlated with the exposed crystallographic planes and the Co^{3+}/Co^{2+} molar ratio.

2.2. Catalytic Evaluation of Co_3O_4 Catalysts

Bai and co-workers [68] reported on porous Co_3O_4 nanowires and nanorods prepared via the hydrothermal or microemulsion method in the presence of PEG or CTAB. The Co_3O_4-HT-PEG and Co_3O_4-HT-CTAB catalysts are porous cubic Co_3O_4 nanowires, whereas the Co_3O_4-ME-CTAB catalyst consists of porous cubic nanorods. The specific surface areas of the porous Co_3O_4 catalysts were in the range of 47–51.7 m^2 g^{-1}, and that of the bulk

Co_3O_4 was 8 m^2 g^{-1}, much lower than that of Co_3O_4-HT-CTAB (51.7 m^2 g^{-1}). In terms of catalytic performance, the porous Co_3O_4-HT-CTAB sample demonstrated better catalytic activity than the other porous Co_3O_4 catalysts and much better activity compared to the nonporous bulk counterpart. The catalytic activity followed the order: Co_3O_4-HT-CTAB > Co_3O_4-HT-PEG > Co_3O_4-ME-CTAB > Co_3O_4-HT> Co_3O_4-Bulk. The lattice spacing (d values) shown in Figure 1 (inset HRTEM) of the Co_3O_4-HT-CTAB catalyst was found to be 0.28 and 0.47 nm, which are relatively close to those of the {220} and {111} lattice planes of the Co_3O_4 catalysts. The lattice spacing of the other porous Co_3O_4 catalysts was 0.28 nm, which was attributed to the {220} lattice plane corresponding to the surface-exposed Co^{3+}. As shown in Figure 1, the Co_3O_4-HT-CTAB catalyst exhibited higher specific activity. These results could be associated with the mixed surface-exposed lattice plane {220}/{111}, which is attributed to the Co^{3+}/Co^{2+} ratio. This correlation is further supported by the higher initial H_2 consumption rate of Co_3O_4-HT-CTAB during TPR (where initial H_2 consumption stands for <25% of oxygen consumption in cobalt oxide), indicating that the molar ratio of Co^{3+}/Co^{2+} was higher for that sample.

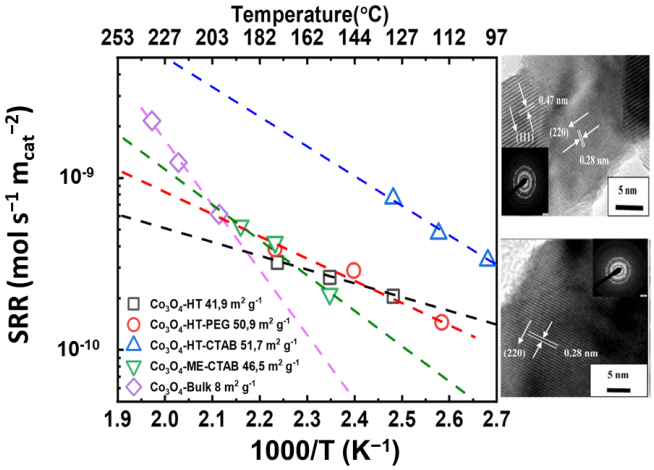

Figure 1. Specific reaction rate (SRR) vs. 1000/T (K^{-1}) vs. temperature (°C) for □ Co_3O_4-HT, ○ Co_3O_4-HT-PEG, △ Co_3O_4-HT-CTAB, ▽ Co_3O_4-ME-CTAB, and ◇ bulk Co_3O_4 (Inset: typical HRTEM images of the studied catalysts (calculated with data from [68]).

Yang et al. [69] employed a modified solvothermal technique to create porous cube-aggregated monodisperse Co_3O_4 microspheres with a specific surface area of 17.4 m^2 g^{-1}. Meanwhile, they prepared bulk Co_3O_4 containing nano/macroparticles after the thermal decomposition of cobalt nitrate precursor at 600 °C with a specific surface area of 8.4 m^2 g^{-1}. Both Co_3O_4 catalysts featured solely the crystallographic {111} plane corresponding to surface-exposed Co^{2+} (Figure 2, inset). The Co_3O_4 microspheres showed better catalytic activity than the bulk Co_3O_4 catalyst, with $T_{100\%}$ at 300 and 340 °C, respectively. As shown in Figure 2, both catalysts show similar specific activities. This result can be attributed to the same exposed lattice plane for both samples, {111}, which corresponds to the surface-exposed Co^{2+}. In addition, an XPS analysis revealed that the catalysts did not show a remarkable change in the surface Co^{3+}/Co^{2+} ratio. Additionally, it should be noted that the consumption of H_2 calculated from the H_2-TPR experiments did not align with the Co^{3+}/Co^{2+} molar ratio determined via the XPS analysis.

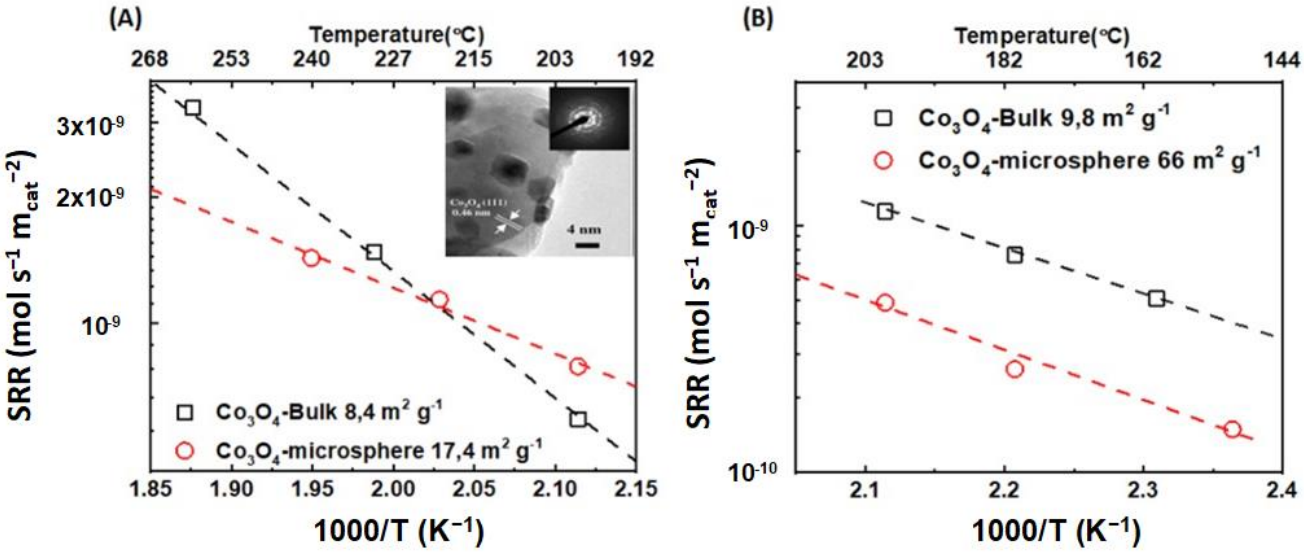

Figure 2. (**A**) Specific reaction rate (SRR) vs. 1000/T (K^{-1}) vs. temperature (°C) for □ bulk Co_3O_4 and ○ bulk Co_3O_4 microspheres (Inset: indicative HRTEM image for the Co_3O_4 microsphere) [69]. (**B**) Specific reaction rate (SRR) vs. 1000/T (K^{-1}) vs. temperature (°C) for □ bulk Co_3O_4 and ○ Co_3O_4 microspheres (calculated with data from [70]).

Wang et al. [70] prepared a nanoplate-aggregate microspherical Co_3O_4 catalyst via an ethylenediamine-assisted hydrothermal method. The catalyst had a cubic crystal structure and comprised nanoplate-aggregate microspheres with a specific surface area of 66 m^2 g^{-1}. For comparison, the authors prepared bulk Co_3O_4 after the thermal decomposition of the cobalt nitrate precursor at 600 °C. The obtained catalyst exhibited a specific surface area of 9.8 m^2 g^{-1}. The Co_3O_4 microspheres displayed better catalytic activity than the bulk Co_3O_4. This result is mainly due to the higher specific surface area of the Co_3O_4 microsphere catalyst. However, the Co_3O_4 bulk catalyst, as shown in Figure 2B, has a higher specific activity than the Co_3O_4 microsphere catalyst. The authors observed that the Co^{3+}/Co^{2+} molar ratio of the Co_3O_4 microspheres was lower than that of the bulk Co_3O_4, indicating a higher surface concentration of Co^{3+} for the latter. From H_2-TPR, the H_2 consumption of the bulk Co_3O_4 was higher than that of the Co_3O_4 microspheres, showing that the molar ratio of Co^{3+}/Co^{2+} was higher in the bulk Co_3O_4, which is in agreement with the XPS results. Hence, the increased specific activity of the Co_3O_4 bulk catalyst could be correlated with the increased molar ratio of Co^{3+}/Co^{2+}. It should be noted that there were no available HRTEM data to retrieve information about the exposed crystallographic planes and correlate it with the specific activity in that work.

In addition, Liu et al. [71] reported on a meso-Co_3O_4 catalyst with a specific surface area of 94 m^2 g^{-1}, which was prepared using a KIT-nanocasting method. For comparison, a bulk Co_3O_4 catalyst with a specific surface area of 8 m^2 g^{-1} was prepared via the thermal decomposition of a nitrate salt precursor at 700 °C. Once again, the higher the specific surface area of the catalyst, the higher the catalytic activity. Specifically, meso-Co_3O_4 achieved complete conversion of toluene at 220 °C, whereas bulk Co_3O_4 achieved this at 320 °C. According to Figure 3, the calculation and extension of the specific reaction rates at comparable temperatures for the two samples led to similar specific activities, with the bulk Co_3O_4 catalyst being slightly better at low temperatures. In accordance with the previous studies, the bulk Co_3O_4 catalyst has a higher Co^{3+}/Co^{2+} molar ratio and higher H_2 consumption compared to the meso-Co_3O_4 catalyst. No HRTEM data were reported for the selected catalysts.

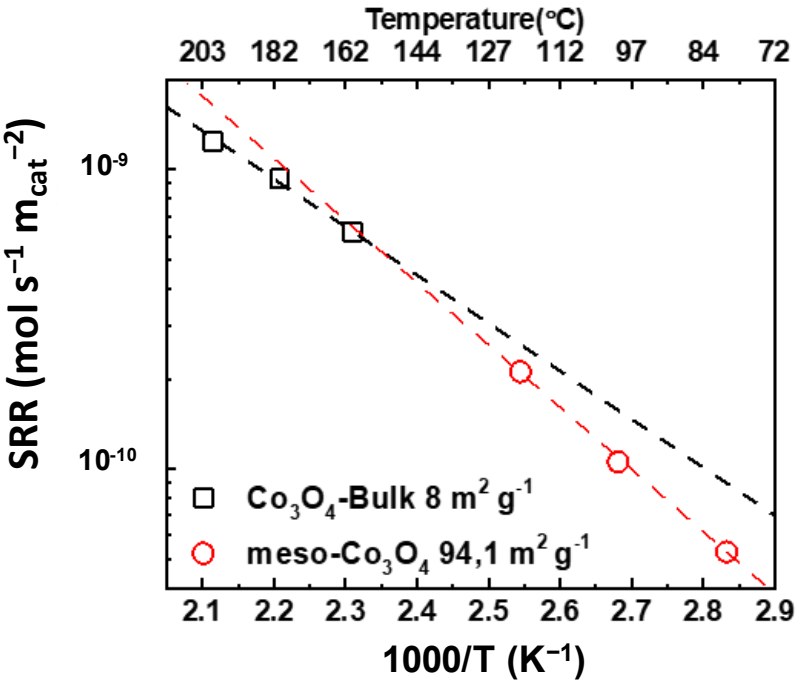

Figure 3. Specific reaction rate (SRR) vs. 1000/T (K^{-1}) vs. temperature (°C) for □ bulk Co_3O_4 and ○ meso-Co_3O_4 (calculated with data from [71]).

Liu and co-workers [72] prepared a Co_3O_4 catalyst by calcinating MOFs-templated precursors. The catalyst showed a higher specific surface area (94.1 m^2 g^{-1}) compared to the reference sample prepared via the precipitation method (66.2 m^2 g^{-1}). The catalysts were evaluated in the total oxidation of toluene, where the Co_3O_4-MOF catalyst exhibited higher catalytic activity on a unit mass basis. The normalization of the reaction rate on a specific surface area basis led to similar specific reaction rates for both samples (Figure 4). According to HRTEM images for the Co_3O_4-MOF sample, the crystallographic planes observed were the {111} and the {220}, attributed to Co^{2+} and Co^{3+}, respectively. No HRTEM data were given for the bulk catalyst. Additionally, neither catalyst was characterized via XPS, and thus no conclusion can be drawn for the surface composition of the catalysts.

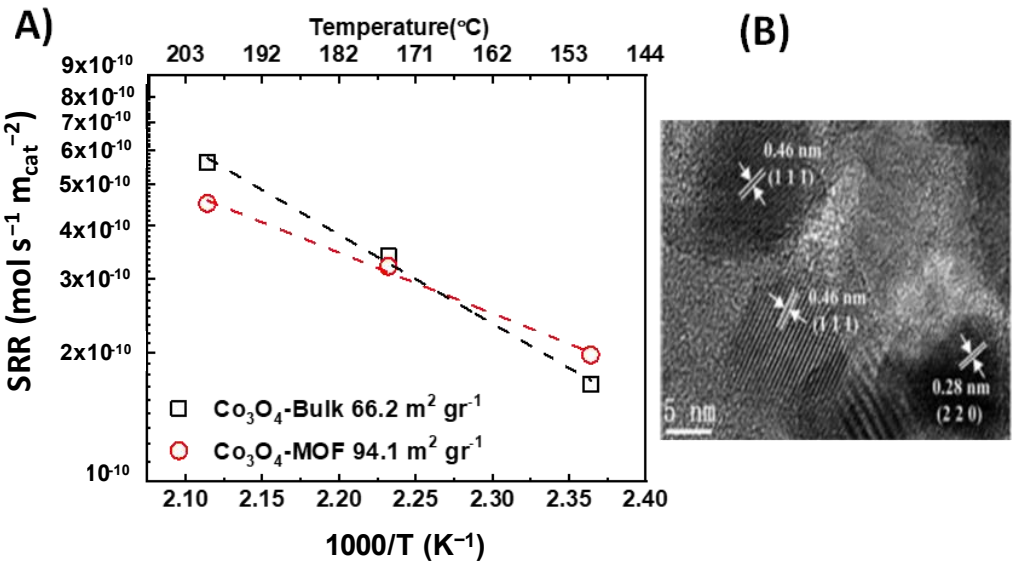

Figure 4. (**A**) Specific reaction rate (SRR) vs. 1000/T (K^{-1}) vs. temperature (°C) for □ bulk Co_3O_4 and ○ Co_3O_4-MOF; (**B**) HRTEM image for Co_3O_4-MOF catalyst (calculated with data from [72]).

Co_3O_4 catalysts with different morphologies and exposed crystallographic planes were successfully synthesized by Ren et al. [73] via a hydrothermal process without a surfactant. After the thermal decomposition of the cobalt precursor carried out through the hydrothermal method, 3D hierarchical cubes-stacked Co_3O_4 microspheres (catalyst C), 3D hierarchical plate-stacked Co_3O_4 flowers (catalyst P), 3D hierarchical needle-stacked Co_3O_4 spheres with an urchin-like structure (catalyst N), and 3D hierarchical sheets-stacked fan-shaped Co_3O_4 (catalyst S) were obtained. The specific surface area of the catalysts was 83.1, 58.8, 25.9, and 53.2 $m^2\ g^{-1}$ for catalysts C, P, N, and S, respectively.

The HRTEM images in Figure 5B confirmed that the crystallographic planes that were primarily exposed for the catalysts C, P, N, and S were the {111}, {110}, {110}, and {112} planes, respectively. Catalyst C has a larger specific surface area than the other catalysts. The catalytic activity for the total oxidation of toluene increased as follows: C > P > N > S. On the other hand, the specific reaction rate at conversions below 20% for the Co_3O_4 catalysts followed the order C = P = N >> S. The unusually low specific activity shown in Figure 5A for the Co_3O_4-S is attributed to the lower molar ratio of Co^{3+}/Co^{2+} from XPS and hydrogen consumption from the H_2-TPR analysis, or/and to the preferred exposed crystallographic plane, {112}. It would be a serious omission not to mention that the Co_3O_4-C catalyst presented a higher molar ratio of Co^{3+}/Co^{2+} after the XPS and H_2-TPR analyses. Nonetheless, the specific reaction rate did not significantly differ from the other catalysts (Figure 5).

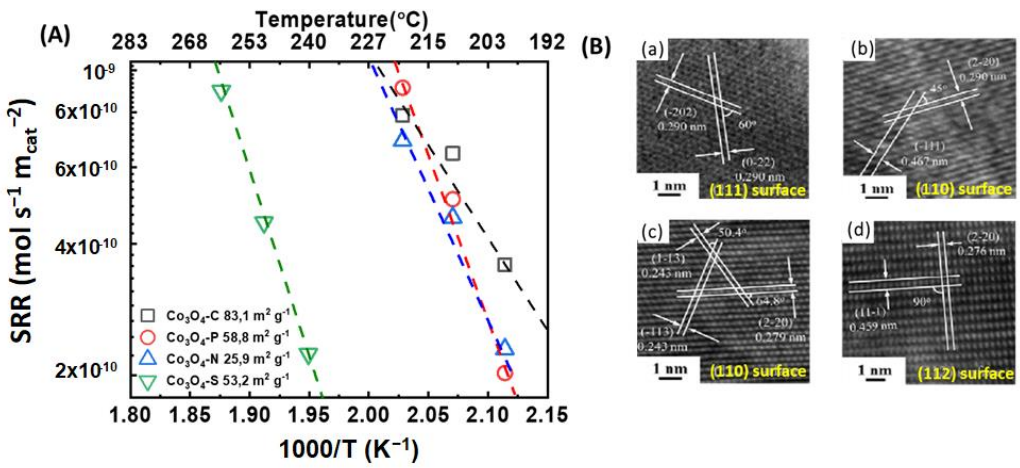

Figure 5. (**A**) Specific reaction rate (SRR) vs. 1000/T (K^{-1}) vs. temperature (°C) for □ Co_3O_4-C, ○ Co_3O_4-P, △ Co_3O_4-N, and ▽ Co_3O_4-S. (**B**) HRTEM images for (**a**) Co_3O_4-C,(**b**) Co_3O_4-P, (**c**) Co_3O_4-N, and (**d**) Co_3O_4-S (calculated with data from [73]).

On the other hand, Liu and co-workers [74] reported on the controlled synthesis of 3D hierarchical Co_3O_4 catalysts with different morphologies. The morphology of the Co_3O_4 catalysts could be tuned by simply changing the calcination temperature. For a deeper understanding of the structures of the obtained Co_3O_4 catalysts, the authors performed HRTEM analyses of the exposed crystallographic planes of the U-80 and S-160 catalysts, as displayed in Figure 6. The specific surface areas of the U-80, US-120, and S-160 catalysts were 38.7 $m^2\ g^{-1}$, 30.2 $m^2\ g^{-1}$, and 26.7 $m^2\ g^{-1}$, respectively. The major exposed planes for the catalyst U-80 were the {111} planes. In contrast, for S-160, the dominant exposed planes were the {110} planes. The evaluation of the catalysts in the complete oxidation of toluene and the meta-analysis of the extracted data demonstrated that the catalytic activity both on a unit mass basis and per surface area followed the order: S-160 > US-120 ≈ U-80. The increased specific activity of the S-160 catalyst, as shown in Figure 6, can be attributed to the exposed {110} planes and the notable change in the molar ratio of Co^{3+}/Co^{2+} from XPS and H_2-TPR, compared with the other catalysts.

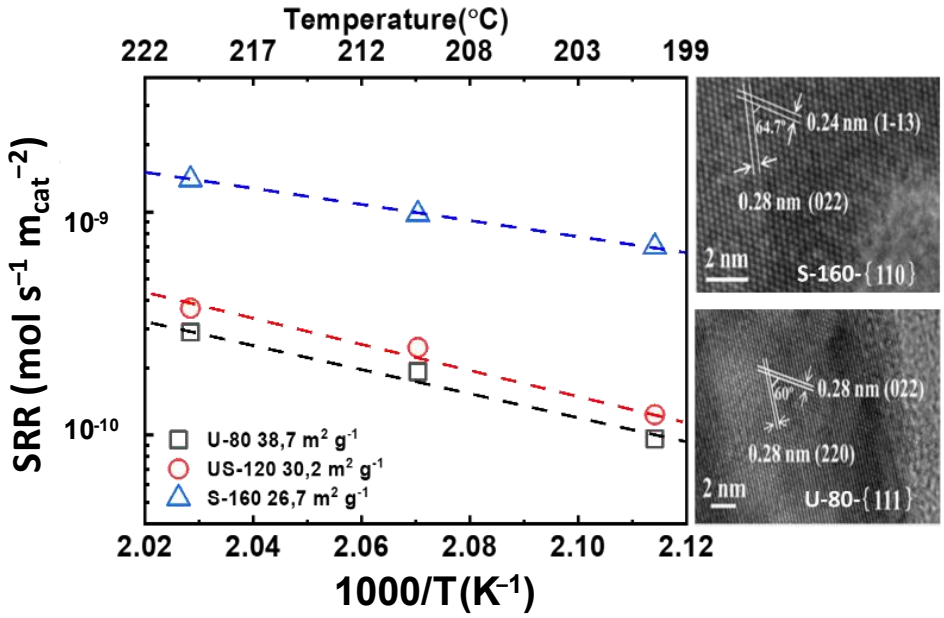

Figure 6. Specific reaction rate (SRR) vs. 1000/T (K^{-1}) vs. temperature (°C) for □ U-80, ○ US-120, and △ US-160: HRTEM image for U-160 and U-80 (calculated with data from [74]).

A series of Co_3O_4 catalysts, such as dumbbell-brush-type mesoporous nanosheets and nanorods, were successfully prepared by Xu et al. [75]. The specific surface areas of Co_3O_4-D, Co_3O_4-S, and Co_3O_4-R were 50, 35, and 26 m^2 g^{-1}, respectively. Co_3O_4-D had a porous dumbbell-brush-type shape with self-assembled nanorods, and as shown in Figure 7. A lattice spacing of 0.280 nm was observed, which can be indexed to the {220} plane of the Co_3O_4 phase. Co_3O_4-S, on the other hand, displays a hexagonal nanosheet morphology. When examining the HRTEM images in Figure 7, it is clear that the nanosheet primarily exposed the {220} facets. In addition, the dominant facets observed for the Co_3O_4-R nanorods were the {220}.

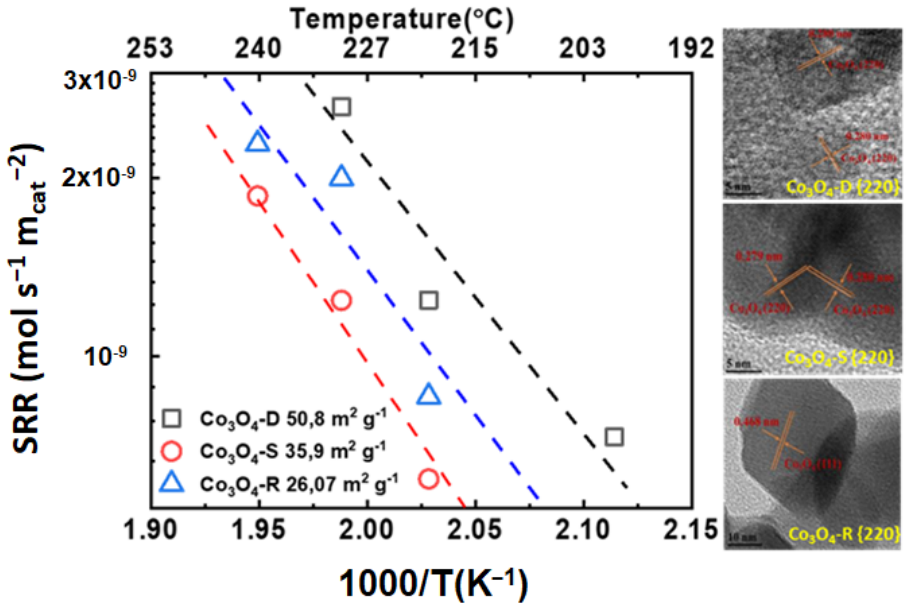

Figure 7. Specific reaction rate (SRR) vs. 1000/T (K^{-1}) vs. temperature (°C) for □ Co_3O_4-D, ○ Co_3O_4-S, and △ Co_3O_4-R, HRTEM images: Co_3O_4-D, Co_3O_4-S, and Co_3O_4-R (calculated with data from [75]).

The aforementioned catalysts were evaluated for the complete oxidation of toluene. It can be observed that the difference in the specific surface area of the Co_3O_4 catalysts strongly influences their catalytic activity. More specifically, Co_3O_4-D had the highest specific surface area and was the best-performing catalyst both in terms of activity and specific activity. Taking into account that all the samples had the same exposed {220} facet, no conclusion can be drawn from the HRTEM results. Nevertheless, according to the XPS and H_2-TPR analyses, the higher specific reaction rate of Co_3O_4-D could be linked with the higher molar ratio of Co^{3+}/Co^{2+} compared to the Co_3O_4-S and Co_3O_4-R catalysts.

Figure 8 depicts a summary of the specific reaction rates attained for the examined Co_3O_4 catalysts (conversions <20%) in the present review. A summary of the catalytic materials, their main physicochemical properties, and specific activity is given in Table 1. The catalysts were synthesized with various methods and exhibited different specific surface areas in the range of 8–100 $m^2\ g^{-1}$, different facets, and different Co^{3+}/Co^{2+} molar ratios. The catalytic evaluation was performed for the complete oxidation of toluene. Based on the Arrhenius plots presented in Figure 8A, the Co_3O_4 catalysts attain specific reaction rates ranging typically from 9.5×10^{-11} to 1.6×10^{-9} mol $s^{-1}\ m^{-2}$, irrespective of the synthesis method and specific surface area. The samples Co_3O_4-HT-CTAB and Co_3O_4-S constitute the obvious exceptions, with specific reaction rates of 3.3×10^{-9} and 1×10^{-11} mol $s^{-1}\ m^{-2}$, respectively, after extrapolating the Arrhenius plots to 200 °C for comparison with the rest of the samples. For a better visualization of the data, the specific reaction rates obtained at 200 °C were plotted as a function of the specific surface area of the studied catalysts (Figure 8B). If the samples Co_3O_4-HT-CTAB and Co_3O_4-S are not taken into account, it is apparent that the specific surface area does not significantly affect the specific reaction rates observed for the oxidation of toluene over Co_3O_4 catalysts. The calculated specific reaction rates are scattered within the 1×10^{-10}–1×10^{-9} mol $s^{-1}\ m^{-2}$ range with no obvious trend for values of specific surface area from 8 to 94 $m^2\ g^{-1}$. Nevertheless, the variations observed in the specific rates are in the order of 3–7 times if Co_3O_4-HT-CTAB and Co_3O_4-S are excluded, and up to 330 times if these samples are included. Hence, it can be concluded that the specific surface area does not affect, to a significant extent, the specific activity of Co_3O_4 catalysts for the oxidation of toluene, at least in the S_{BET} region studied. However, considering the variations in the specific reaction rates, it can be deduced that factors such as the morphology and induced exposure of different facets, as well as the surface concentration and oxidation state of cobalt cations, play a key role in the specific activity of the samples.

Table 1. Summary of the Co_3O_4 catalysts chosen for the meta-analysis, including the preparation methods, their main physicochemical properties (S_{BET}, morphology and Co^{3+}/Co^{2+} ratio), and the specific reaction rates attained at 200 °C for the total oxidation of toluene.

Catalyst	Preparation Method	Morphology	S_{BET} ($m^2\ g^{-1}$)	Co^{3+}/Co^{2+} Ratio	GHSV (ml $g^{-1}\ h^{-1}$)	SRR (200 °C) ($\times 10^{-10}$ mol $s^{-1}\ m^{-2}$)	Ref.
Co_3O_4-HT	hydrothermal	irregular	41.9	2.13	20,000	4.00	[68]
Co_3O_4-HT-PEG	hydrothermal	nanowires /nanorods	50.9	2.01	20,000	5.68	[68]
Co_3O_4-HT-CTAB	hydrothermal	nanowires /nanorods	51.7	1.72	20,000	33.4	[68]
Co_3O_4-ME-CTAB	microemulsion	nanowires /nanorods	46.5	2.05	20,000	7.02	[68]
Co_3O_4-microsphere	solvothermal	microspheres	17.4	1.36	20,000	6.36	[69]

Table 1. *Cont.*

Catalyst	Preparation Method	Morphology	S_{BET} (m^2 g^{-1})	Co^{3+}/Co^{2+} Ratio	GHSV (ml g^{-1} h^{-1})	SRR (200 °C) ($\times 10^{-10}$ mol s^{-1} m^{-2})	Ref.
Co_3O_4-bulk	thermal decomposition	irregular	8.4	1.47	20,000	5.86	[69]
Co_3O_4-microsphere	hydrothermal	microspheres	66	1.44	20,000	4.88	[70]
Co_3O_4-bulk	thermal decomposition	polyhedra	9.8	1.65	20,000	11.2	[70]
Meso-Co_3O_4	KIT-nanocasting	3D ordered mesoporous	94.1	1.33	20,000	16.3	[71]
Co_3O_4-bulk	thermal decomposition	-	8	1.74	20,000	12.4	[71]
Co_3O_4-MOF	MOF precursors calcination	distorted nanocubes	94.1	-	60,000	4.53	[72]
Co_3O_4-bulk	precipitation	-	66.2	-	60,000	5.64	[72]
Co_3O_4-C	hydrothermal	3D hierarchical cubes	83.1	1.67	48,000	3.58	[73]
Co_3O_4-P	hydrothermal	plates	58.8	1.02	48,000	2.00	[73]
Co_3O_4-N	hydrothermal	3D hierarchical needles	25.9	1.02	48,000	2.36	[73]
Co_3O_4-S	hydrothermal	3D hierarchical sheets	53.2	1.02	48,000	0.10	[73]
U-80	hydrothermal	urchin-like	38.7	0.31	60,000	0.96	[74]
US-120	hydrothermal	urchin/shale-like	30.2	0.38	60,000	1.23	[74]
S-160	hydrothermal	shale-like	26.7	0.61	60,000	6.90	[74]
Co_3O_4-D	hydrothermal	dumbbell-brush-type	50.8	2.14	60,000	7.18	[75]
Co_3O_4-R	solvothermal	mesoporous nanorods	26	1.62	60,000	3.27	[75]
Co_3O_4-S	sol-gel	mesoporous nanosheets	35.9	1.95	60,000	2.02	[75]

Additionally, the apparent activation energies (E_{app}) of all the studied catalysts were calculated from the corresponding Arrhenius plots, and they were found to vary widely from 15 ± 3 kJ mol^{-1} to 157 ± 2 kJ mol^{-1}.

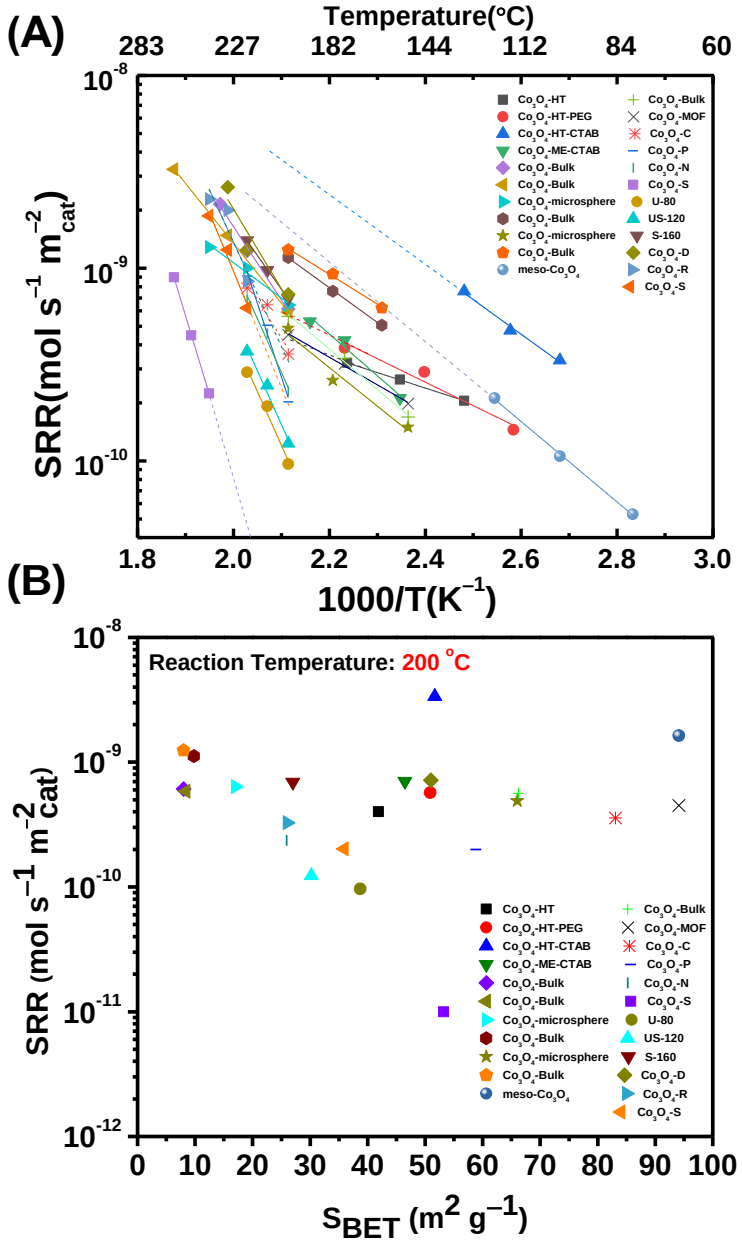

Figure 8. (**A**) Summary of the specific reaction rates (SRRs) for toluene oxidation vs. 1000/T (K^{-1}) vs. temperature (°C) and (**B**) effect of specific surface area on the specific reaction rates at 200 °C for all the studied catalysts.

3. Co_3O_4 Catalysts and Their Physicochemical Characterization

The physicochemical characterization of the catalytic materials is essential for a deep understanding of their catalytic performance. The correlation of the structural, textural, and chemical properties of the catalysts with the catalytic evaluations will enable the rational design and improvement of their activity. In the following section, the typical physicochemical techniques used for the detailed characterization of Co_3O_4 will be analyzed.

3.1. Powder X-ray Diffraction (PXRD)

Usually, the catalysts are scanned in the 2θ range of 10°–80° and show eleven diffraction peaks related to face-centered cubic spinel Co_3O_4 (Fd3m space group) (Figure 9A). The 2θ diffraction peaks are 19.1° (111), 31.2° (220), 36.8° (311), 38.5° (222), 44.7° (400), 55.6° (422), 58.9° (511), 64.7° (440), 73.6° (620), 76.8° (533), and 77.7° (622).

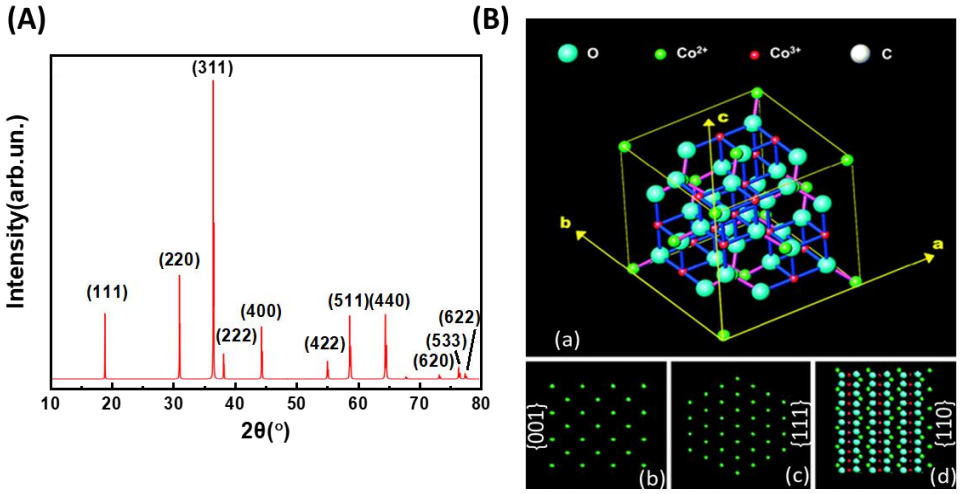

Figure 9. (**A**) Typical PXRD diagram for Co_3O_4, (**B**) (**a**) spinel structure of Co_3O_4 crystal, and (**b**–**d**) surface atomic configurations of the {001} (**b**), {111} (**c**), and {110} (**d**) planes (adapted with some modifications from [42] with permission from RCS).

The significant broadening of the diffraction peaks reveals a nanometric particle structure. The average crystallite size is calculated using the Scherrer equation (Equation (5)) [76].

$$d_{PXRD} = \frac{K * \lambda}{\beta * cos\Theta} \quad (5)$$

where d_{PXRD} is the crystallite diameter, K is a constant with the value of 0.941, λ is the radiation wavelength, β is the peak width at half maximum in radians, and θ is the reflection angle. In addition, the lattice parameters of the catalysts can be calculated from a Rietveld refinement analysis of the PXRD patterns. From the Rietveld analysis, the microstrain related to the method and temperature of synthesis of the catalysts can be drawn. Figure 9B [42] shows a typical cubic spinel structure schematic, with Co^{2+} ions in the tetrahedral interstices and Co^{3+} ions in the octahedral interstices. In this standard spinel structure, Co^{2+} cations occupy 8a sites with tetrahedral coordination, whereas Co^{3+} cations are located at 16d sites with octahedral coordination, according to the formula $[Co^{2+}]_{8a}$ $[Co^{3+}]_{16d}$ [77,78].

The Co^{2+} cations correspond to 8a sites and form a diamond-like lattice, consisting of two displaced face-centered sublattices tetrahedrally surrounded by the four nearest Co^{2+} neighbors. The close-packed planes were {001}, {111}, and {110}, and their surface atomic configurations are shown in Figure 9b–d. Thus, the {001} and {111} planes contain only Co^{2+} cations, whereas the {110} plane primarily consists of Co^{3+} cations [42]. An increase in the crystallite size leads to a decrease in the exposed surface area (per unit volume or mass), which is supported by the example shown in Table 2.

Table 2. Data from N_2 physisorption and P_{XRD}, adapted from reference [79].

Catalysts	S_{BET} (m^2 g^{-1})	d_{PXRD} (nm)
CoDP	82	11.9
CoAP	37	21.6

3.2. X-ray Photoelectron Spectroscopy (XPS)

XPS is an essential technique for examining the surface chemical composition of Co_3O_4. As illustrated in Figure 10, a typical XPS spectrum shows the splitting of Co $2p_{3/2}$ and Co $2p_{1/2}$ at 781 and 795 eV, respectively. These show the surface species combined with the shake-up satellite located at a higher binding energy of 6.7 eV from the main peak. The estimated $2p_{3/2}$–$2p_{1/2}$ spin–orbit splitting is 15.1 eV for Co_3O_4. Octahedral Co^{3+} is

located at 779.6 eV, and tetrahedral Co^{2+} is located at 780.7 eV, with spin–orbit splitting at 794.5 eV and 796 eV, respectively. These results indicate the existence of surface Co^{3+} and Co^{2+} species [80]. After background correction and peak deconvolution, the Co^{3+}/Co^{2+} molar ratio of Co_3O_4 on the surface can be expressed, which could play a crucial role in oxidation catalysis. With differences in coordination, oxidation states, and bond lengths of different Co_3O_4 catalysts, it is expected that differences exist in the chemical shifts, multiple splits, shake-up structures, and valence band structures.

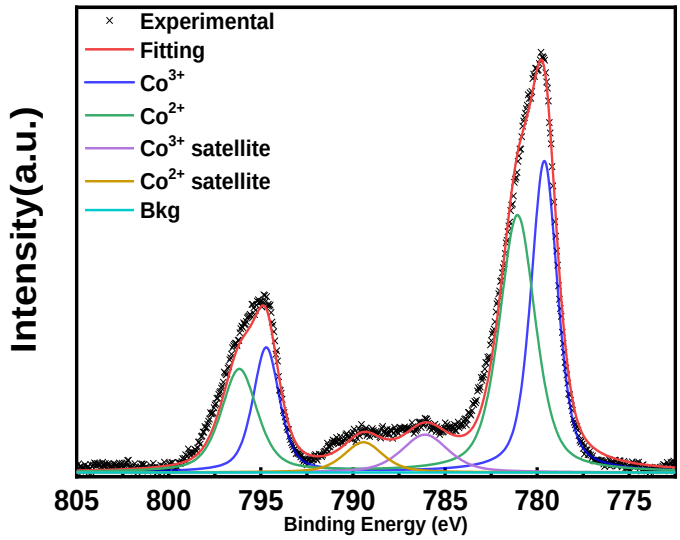

Figure 10. Typical Co 2p XPS spectrum.

The deconvolution of the O1s spectrum of Co_3O_4 indicates oxygen species with binding energies around 529.9, 531.6, and 533.5 eV, which are due to the surface lattice oxygen (O_{latt}), the surface hydroxyl species (O_{ads}), and the adsorbed water species, respectively [81]. A high relative O_{ads}/O_{latt} concentration ratio on the Co_3O_4 surface did not enhance catalytic oxidation. It should be highlighted that a material with a higher Co^{3+}/Co^{2+} molar ratio shows a lower O_{ads}/O_{latt} molar ratio.

Figure 11A shows the surface Co^{3+}/Co^{2+} molar ratio calculated from the XPS data as a function of the specific surface area (S_{BET}) for all surveyed catalysts. The Co^{3+}/Co^{2+} molar ratio varies from 1.1 to 3.2 for all the catalysts with an S_{BET} in the range 8–94 $m^2\ g^{-1}$. More specifically, twelve of the catalysts with an S_{BET} below 40 $m^2\ g^{-1}$ show a Co^{3+}/Co^{2+} molar ratio from 1.1 to 1.7, while five of the catalysts with an S_{BET} of 42–58 $m^2\ g^{-1}$ show a Co^{3+}/Co^{2+} molar ratio from 1.8 to 2.1. Moreover, eight of the catalysts with an S_{BET} of 8–80 $m^2\ g^{-1}$ present a Co^{3+}/Co^{2+} molar ratio from 2.2 to 3.2. It is worth mentioning that the theoretically expected value of the Co^{3+}/Co^{2+} ratio is two. This difference presented by the research papers studied is probably due to the different synthesis methods and, therefore, the different exposed crystallographic planes.

The correlation between the calculated specific reaction rates (see Figure 8 and Table 1) and the surface Co^{3+}/Co^{2+} molar ratio is illustrated in Figure 11B. It can be deduced that a higher surface concentration of Co^{3+} has a rather positive effect on the specific activity of Co_3O_4 catalysts for the total oxidation of toluene, but the experimental scattering of the results is significant. Therefore, the Co^{3+}/Co^{2+} molar ratio is certainly not the single factor determining the specific reaction rate of the catalysts.

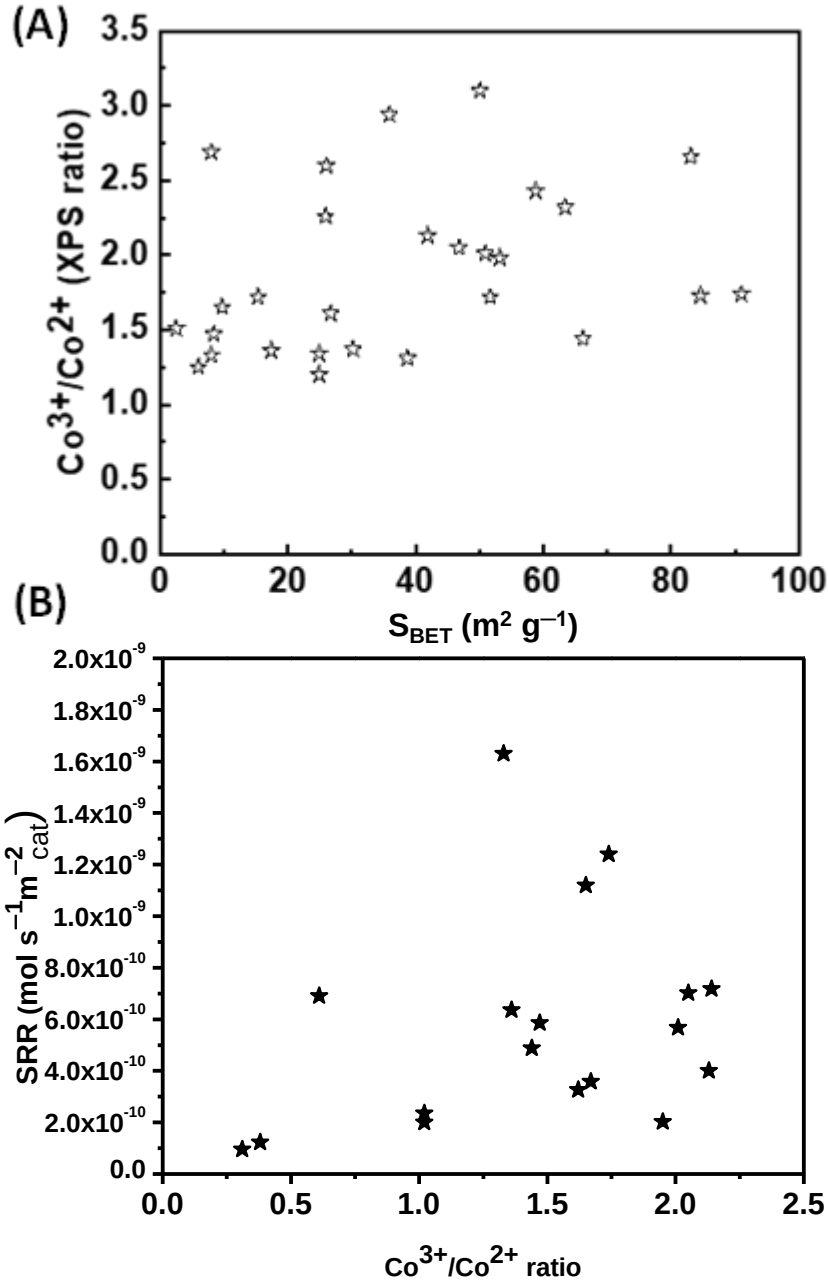

Figure 11. (**A**) Co^{3+}/Co^{2+} molar ratio as determined via XPS analysis as a function of the specific surface area (S_{BET}) for all catalysts and (**B**) specific reaction rates (SRR) as a function of surface Co^{3+}/Co^{2+} molar ratio (prepared from bibliographic data).

3.3. Raman Spectroscopy and Attenuated Total Reflectance Fourier Transmittance Infrared Spectroscopy (ATR-FTIR)

Co_3O_4 Raman spectra consist of five Raman bands, as reported by Dialo et al. [82] and Lei et al. [83], and they are shown in Figure 12A,B. The Raman bands at 194, 480, 520, 619, and 670 cm^{-1} are assigned to the $F_{2g}^{(3)}$, E_g, $F_{2g}^{(1)}$, $F_{2g}^{(2)}$, and A_{1g} modes of the Co_3O_4 spinel structure. The sublattice vibration attributable to octahedral–tetrahedral sites is at a value of 670 cm^{-1}. Any minor variations in this vibration can be associated with a lattice distortion of the spinel system or residual stress. This phenomenon is observed in Figure 12B for Co_3O_4 prepared from different MOF precursors.

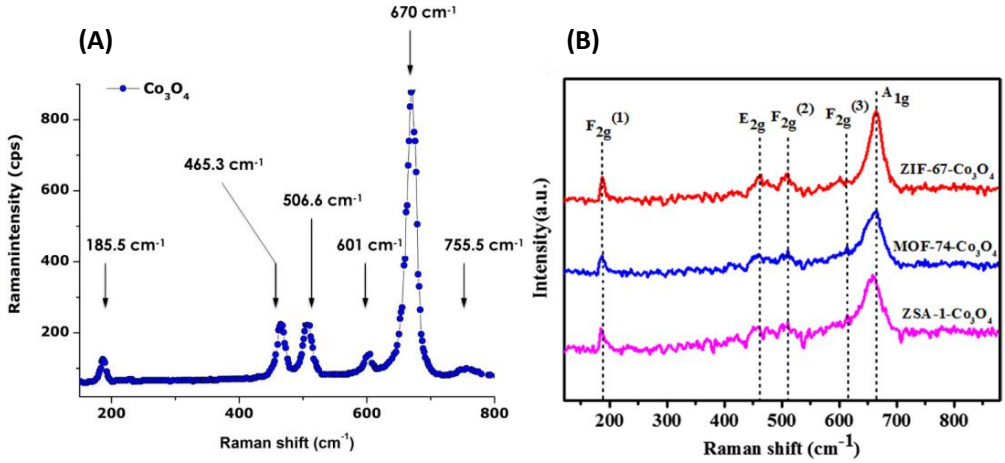

Figure 12. (**A**,**B**) Typical Raman spectra of the annealed Co_3O_4 nanoparticles adapted from refs. [82,83] with permission from Taylors & Francis and Elsevier, respectively.

However, from the ATR, the observed 570 cm^{-1} band is characteristic of the O–Co bond, denoting Co^{3+} at the octahedral site. The 668 cm^{-1} band is attributable to the Co^{2+}–Co^{3+}–O_3 (Co^{2+} in the tetrahedral site) vibration in the spinel lattice. Any asymmetric band at 1627 cm^{-1} is due to the OH groups from adsorbed water. It should be noted that adsorbed water can be easily desorbed at temperatures around 120–150 °C under a gaseous flow.

3.4. Hydrogen Temperature-Programmed Reduction (H_2-TPR)

Temperature-programmed reduction (TPR) is a widely used technique to investigate the reducibility of solid catalysts. TPR involves exposing the catalytic material to a stream of reducing gas, usually H_2, at various temperatures, resulting in a TPR profile, i.e., the reduction rate versus the temperature of the reactor. Qualitatively, the position of the reduction peaks provides information on the ease of reduction of these chemical species, where easier reduction is indicated by the appearance of a peak maximum at a lower temperature. Quantitatively, the amount of hydrogen consumed during the measurement can be compared to a theoretical one to determine the extent of the catalyst reduction. The reduction of the Co_3O_4 catalysts is exemplified in the H_2-TPR profiles by two reduction peaks. The peak at 200–300 °C is due to the reduction of Co_3O_4 to CoO. The peak within the 300–450 °C range is due to the reduction of CoO to metallic Co^0. The theoretical H_2 consumption for the complete reduction of Co_3O_4 to Co^0 is 16.6 mmol g^{-1}. The overall reduction is described by Equations (6) and (7) as follows:

$$Co_3O_4 + H_2 \rightarrow 3CoO + H_2O \quad (6)$$

$$3CoO + 3H_2 \rightarrow 3Co + 3H_2O \quad (7)$$

It is worth mentioning that the peak below 200 °C is attributed to the reduction of oxygenated surface species formed during oxidation pre-treatment [84]. The range of the reduction temperature varies according to the surface area, preparation method, and morphology of the catalysts. Typical H_2-TPR profiles are presented in Figure 13, taken from the work of Zhang et al. [79], Ma et al. [60], and Ren et al. [73].

As depicted in Figure 13A, a slight modification in the precipitation method from Zhang et al. [79] resulted in CoAP having a 2.2 times lower specific surface area compared with CoDP, and thus revealing different crystallite sizes. Furthermore, the difference in material composition results in a difference in the Co^{3+}/Co^{2+} ratio and, finally, in the temperature reduction profile. Figure 13B compares the H_2-TPR profiles of the Co_3O_4 rods (Co_3O_4-R), Co_3O_4 hexagonal plates (Co_3O_4-H), and Co_3O_4 double-sided helianthus discs (Co_3O_4-D). These materials were also synthesized using the hydrothermal method by Ma et al. [60] by adjusting the water/ethanol ratio. In this case, Co_3O_4 with different morpholo-

gies did not show remarkably different H_2-TPR profiles or reduction temperatures. This is possibly because the catalysts have only minor differences in their specific surface area. The main difference was the highest Co^{3+}/Co^{2+} ratio, indicating that more Co^{3+} species were exposed on the surface of the Co_3O_4-B catalyst. This result is probably due to the unique double-sided nanobrush structure of the Co_3O_4-B catalyst.

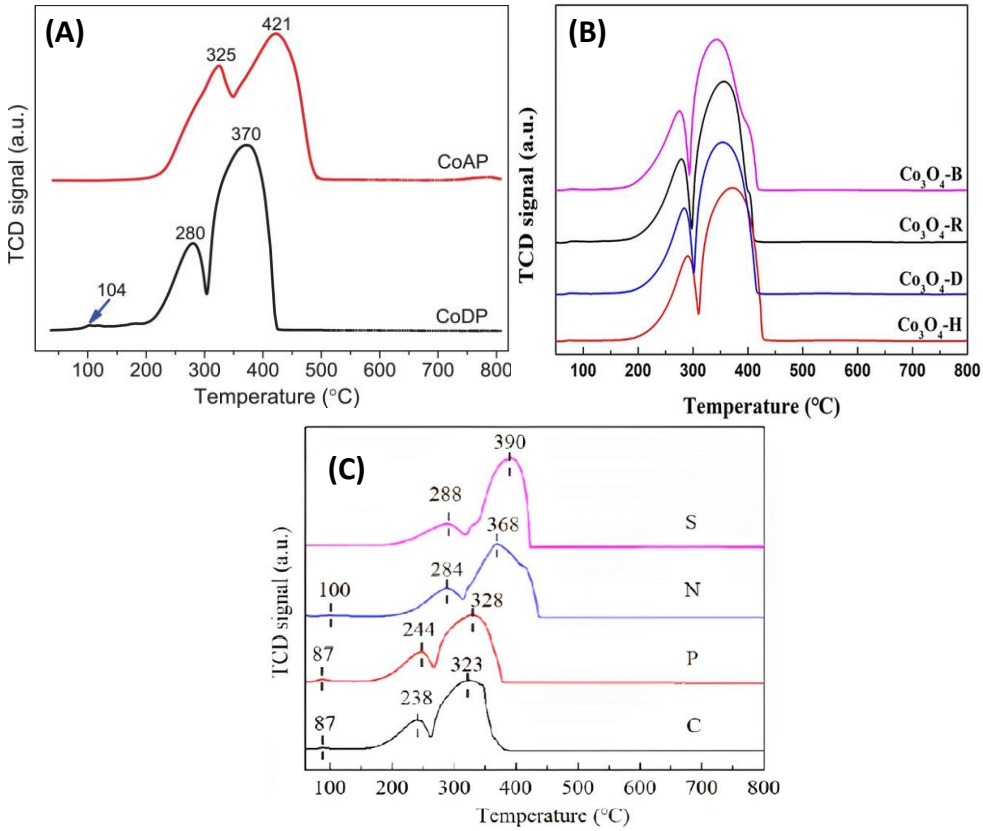

Figure 13. (**A**–**C**) H_2-TPR profiles of Co_3O_4 catalysts (adapted from [79] with permission from Elsevier, from [60] with permission from RSC, and from [73] with permission from RSC, respectively).

Figure 13C shows the H_2-TPR profiles of the hydrothermally synthesized Co_3O_4 catalysts present in the form of cube-stacked microspheres (C catalyst), plate-stacked flowers (P catalyst), needle-stacked double-spheres with an urchin-like structure (N catalyst), and sheet-stacked fan-shaped Co_3O_4 (S catalyst) [73]. According to these H_2-TPR profiles, the catalyst morphology and, therefore, the specific surface area played a significant role compared with the Co^{3+}/Co^{2+} molar ratio. In this case, it is also necessary to note that the C catalyst has a higher S_{BET} of 83 $m^2\ g^{-1}$, those of the S and P catalysts are close to 55 $m^2\ g^{-1}$, and that of the N catalyst has the lowest value of 30 $m^2\ g^{-1}$. In contrast, the mean crystallite size of the C, P, N, and S catalysts were 16, 18, 30, and 17 nm, respectively. Thus, it was demonstrated that the cube-stacked microspheres (catalyst C) with the highest S_{BET} had slightly lower reduction temperatures.

To summarize, three different H_2-TPR profiles are shown in Figure 13. In all cases, the morphology and S_{BET} played an essential role. It is observed that the main factor in the profile and the temperature of reduction in Co_3O_4 is the Co^{3+}/Co^{2+} molar ratio. It should be noted that higher Co^{3+}/Co^{2+} ratio values resulted in an alteration of the reduction profile. Moreover, it is evident that the reduction of CoO to Co is highly dependent on the Co_3O_4 morphology.

3.5. Oxygen Temperature-Programmed Desorption (O_2-TPD)

The presence of oxygen, either adsorbed, lattice-bound, or in gaseous form, is a critical factor in the oxidation reactions that take place over transition metal oxide catalysts. In this context, the O_2 Temperature Programmed Desorption (O_2-TPD) technique is a valuable tool for assessing oxygen storage and mobility, and it is capable of discerning between various oxygen species on the catalytic surface. Typical TPD profiles (O_2 desorption rate vs. temperature) comprise one or more peaks attributed to different adsorption strengths of oxygen species. The representative O_2-TPD profiles of the Co_3O_4 catalysts are shown in Figure 14. Figure 14A refers to the Co_3O_4/KIT-6 ordered mesoporous catalysts prepared using the impregnation method. These experiments were performed on Co_3O_4 catalysts to explore the relationship between adsorbed oxygen species and the Co_3O_4 surface structure. The O_2-TPD profiles of the transition metal oxides showed that the oxygen species were desorbed within a wide temperature range. The O_2-TPD profiles were divided into three main categories: physically adsorbed oxygen (O_2, ads), chemically adsorbed oxygen (O_2^-/O^-), and lattice oxygen (O^{2-}). It is also worth noting that physically adsorbed oxygen is easily desorbed and can be removed before the start of the O_2-TPD experiment using a pure He flow.

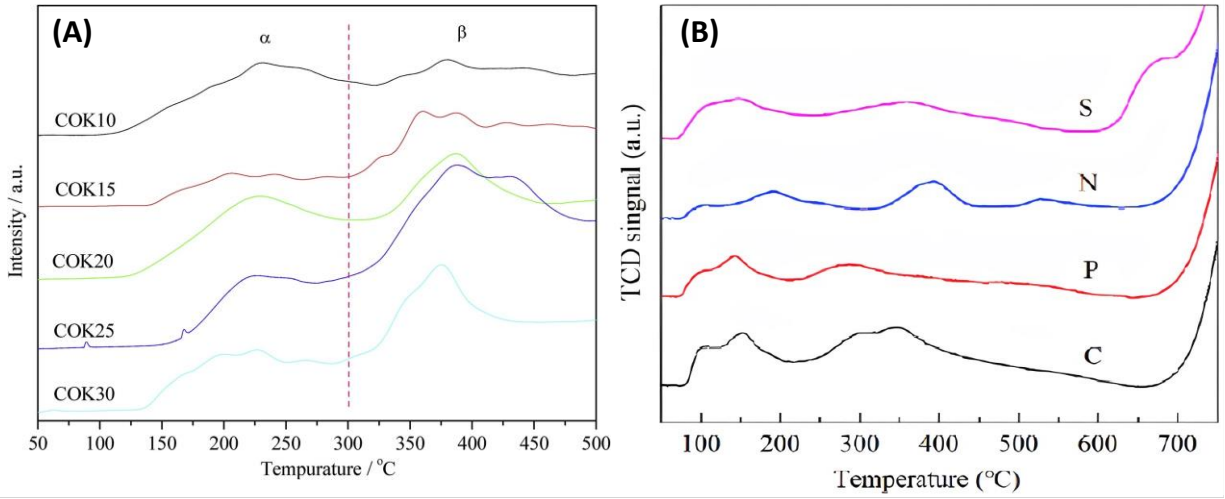

Figure 14. (**A**) O_2-TPD profiles of the COKx catalysts adapted from [85] with permission from Elsevier; (**B**) O_2-TPD profiles of Co_3O_4 catalysts in the form of sheets, needles, plates, and cubes adapted from [73] with permission from RSC.

Chemisorbed oxygen molecules can be desorbed above 100 °C from metal oxides, whereas lattice oxygen is challenging to desorb, and the temperature required is generally close to 500 °C. In Figure 14A, Xie et al. [85] describe the α and β oxygen desorption regions of Co_3O_4/KIT-6 catalysts. The oxygen desorption peaks in areas α and β belong to the surface desorption of weakly chemisorbed oxygen species and strongly chemisorbed oxygen (O_2^-/O^-) species from oxygen vacancies, respectively.

On the other hand, Ren et al. [73] (Figure 14B) define four kinds of oxygen species that are observed in the temperature ranges of 80–120 °C, 120–450 °C, 450–700 °C, and above 700 °C. The above temperatures could be assigned to molecular oxygen species adsorbed on oxygen vacancies (O_v), surface-adsorbed oxygen ions (O_{ads}), surface lattice oxygen ($O_{latt,s}$), and bulk-phase lattice oxygen ($O_{latt,b}$), respectively. The desorption peak at approximately 100 °C for the C, P, and N catalysts was attributed to the desorption of molecular oxygen. Thus, the O_2-TPD profiles show that the chemisorbed oxygen species can desorb at relatively low temperatures. The desorption profiles varied depending on the preparation method and the catalyst morphology.

3.6. Scanning Electron Microscopy (SEM) and High-Resolution Transmission Electron Microscopy (HRTEM)

Figure 15 presents the SEM and HRTEM images of the Co_3O_4 catalysts prepared using different synthesis methods. In addition, SEM and high-resolution TEM images were used to examine various catalyst morphologies and exposed crystallographic planes, respectively. The HRTEM technique is employed to further study the size distribution of crystallites and the active facets for catalysis. It is worth noting that in most cases, the HRTEM size distribution and the crystallite size calculated from XRD must be comparable.

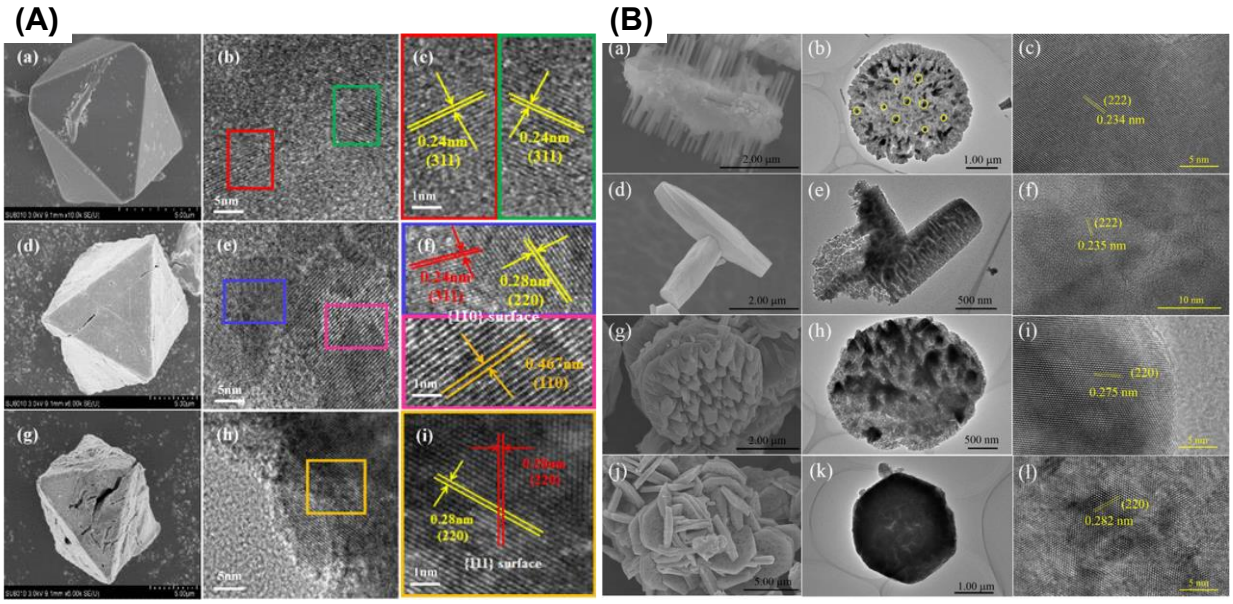

Figure 15. (**A**) SEM images of (**a**) M-X-250, (**d**) M-Co_3O_4-350, and (**g**) M-Co_3O_4-450 and TEM images of the synthesized catalysts, M-X-250 (**b**,**c**), M-Co_3O_4-350 (**e**,**f**), and M-Co_3O_4-450 (**h**,**i**) (adapted from [86]) with permission from Elsevier, and (**B**) SEM and TEM images of the synthesized Co_3O_4 catalysts: (**a**–**c**) Co_3O_4-B, (**d**–**f**) Co_3O_4-R, (**g**–**i**) Co_3O_4-D, and (**j**–**l**) Co_3O_4-H (adapted from [60] with permission from RCS).

Figure 15A shows the HRTEM images of M-Co_3O_4-350 (Figure 15(Ae)), M-Co_3O_4-450 (Figure 15(Ah)), and M-X-250 (Figure 15(Ab)). The lattice spacing in Figure 15Ac for M-X-250 was 0.24 nm, corresponding to the {311} plane. For the M-Co_3O_4-350, the three lattice fringes are shown in Figure 15(Ae,f), which are 0.24 nm, 0.28 nm, and 0.467 nm, and these are derived from the {311}, {220}, and {110} crystallographic planes, respectively. Nevertheless, the {110} plane is the dominant exposed surface for this material. However, M-Co_3O_4-450 (h, i) demonstrates that the {111} plane is the predominant one. From the above data, it is clear that the exposed planes of Co_3O_4 can be manipulated by controlling the Co-MOF calcination temperature. Figure 15A presents the Co-MOF (ZSA-1) materials synthesized through a hydrothermal method. The as-received Co-MOF was used as a precursor to obtain the final catalysts. The precursor was calcined in air at different temperatures (250, 350, and 450) for 1 h. The SEM images in Figure 15(Aa,d,g) present the catalysts obtained after calcination. These Co_3O_4 catalysts exhibited octahedral morphologies with slightly different surfaces depending on the calcination temperature.

The SEM images in Figure 15(Ba,d,g,j) show the double-sided nanobrush Co_3O_4 (Co_3O_4-B), Co_3O_4 rods (Co_3O_4-R), Co_3O_4 hexagonal plates (Co_3O_4-H), and Co_3O_4 double-sided helianthus discs (Co_3O_4-D), which were prepared by tuning the water/ethanol ratio using a hydrothermal method.

Figure 15(Bc,f,i,l) presents the HRTEM images of the aforementioned materials. The Co_3O_4-B lattice spacing in Figure 15(Bc) is 0.234 nm, corresponding to the {222} plane of Co_3O_4-B. In addition, the HRTEM image of the Co_3O_4-R catalyst showed a lattice spacing

of 0.235 nm (Figure 15(Bf)), which corresponds to the {222} plane of Co_3O_4. A {220} crystallographic plane with a d-spacing of 0.275 nm is observed in Figure 15Bi for the Co_3O_4-D catalyst. The HRTEM image in Figure 15Bl shows that the Co_3O_4–H catalysts possessed a {220} plane with a lattice spacing of 0.282 nm. Based on these results, it can be concluded that the exposed facets of the catalysts can be modified by changing their morphology.

4. Designing Co_3O_4 Catalysts

In this section, the preparation methods and the precursors employed to obtain Co_3O_4 catalysts with different textural and structural characteristics are summarized. Several cobalt compounds have been used as precursors to prepare Co_3O_4 for the complete oxidation of VOCs. These include cobalt nitrate hexahydrate [$Co(NO_3)_2{\cdot}6H_2O$], cobalt chloride hexahydrate [$CoCl_2{\cdot}6H_2O$], cobalt sulfate hexahydrate [$Co(SO_4)_2{\cdot}6H_2O$)], cobalt hydroxide [$Co(OH)_2$], cobalt basic carbonate [$2CoCO_3{\cdot}3Co(OH)_2{\cdot}H_2O$], cobalt acetate [$Co(CH_3COO)_2$], and cobalt acetylacetonate ($Co(C_5H_7O_2)_2$). Co-MOFs as precursors have also been a new trend in recent years. From Figure 16, it can be concluded that the most used precursor is cobalt nitrate, employed in 72% of the reported studies, followed by cobalt chloride and cobalt acetate (11% each).

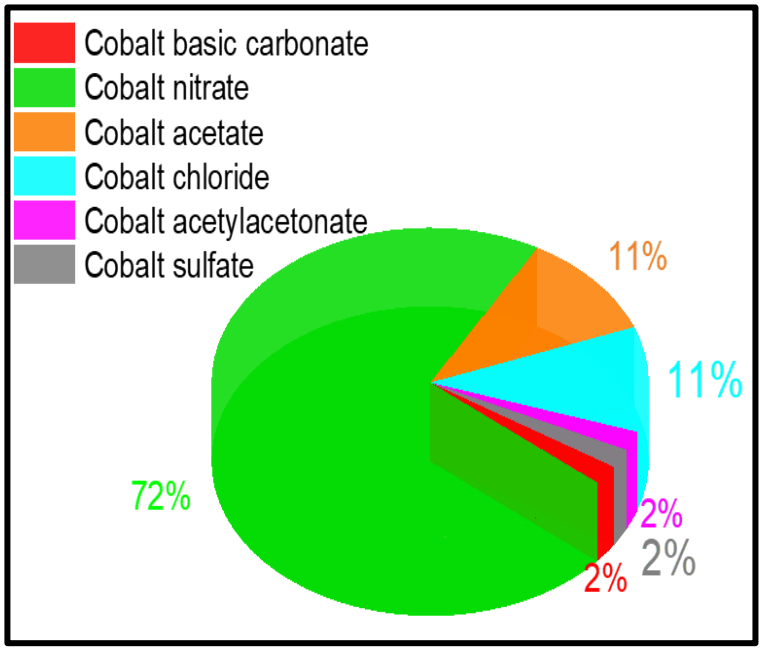

Figure 16. Distribution of the precursors most commonly used for the synthesis of Co_3O_4 catalysts.

The most representative Co_3O_4 synthesis methods are shown in Scheme 2. These include the hydrothermal/solvothermal method [53], the sol–gel process [54], thermal decomposition [24], chemical precipitation, and hard or soft templates [55]. The simple thermal decomposition of a cobalt precursor was used by Rivas et al. [33], Wang et al. [70], Liu et al. [58], Bai et al. [68], and Yan et al. [32]. The thermal decomposition method results in catalysts with a specific surface area in the range 3–82 $m^2\ g^{-1}$, which depends on the calcination temperature, typically 300–700 °C.

Other research groups such as Li et al. [22], Ren et al. [87], Ma et al. [60], Zhang et al. [79], Liu et al. [74], Liotta et al. [88], Ma et al. [89], Fan et al. [90], and Anke et al. [91] employed a precipitation method to prepare Co_3O_4 as a catalyst for complete VOC oxidation. The specific surface area of the produced catalysts varied from 5 to 151 $m^2\ g^{-1}$ depending on the calcination temperature. The employed precipitation agents were, in most cases, urea (CH_4N_2O), hydroxycarbonate (CH_2O_5), sodium carbonate (Na_2CO_3), ammonium hydroxide ($NH_3{\cdot}H_2O$), sodium hydroxide (NaOH), potassium hydroxide

(KOH), ammonium bicarbonate (NH_4HCO_3), potassium bicarbonate ($KHCO_3$), potassium carbonate (K_2CO_3), and oleylamine ($C_2H_2NH_2$).

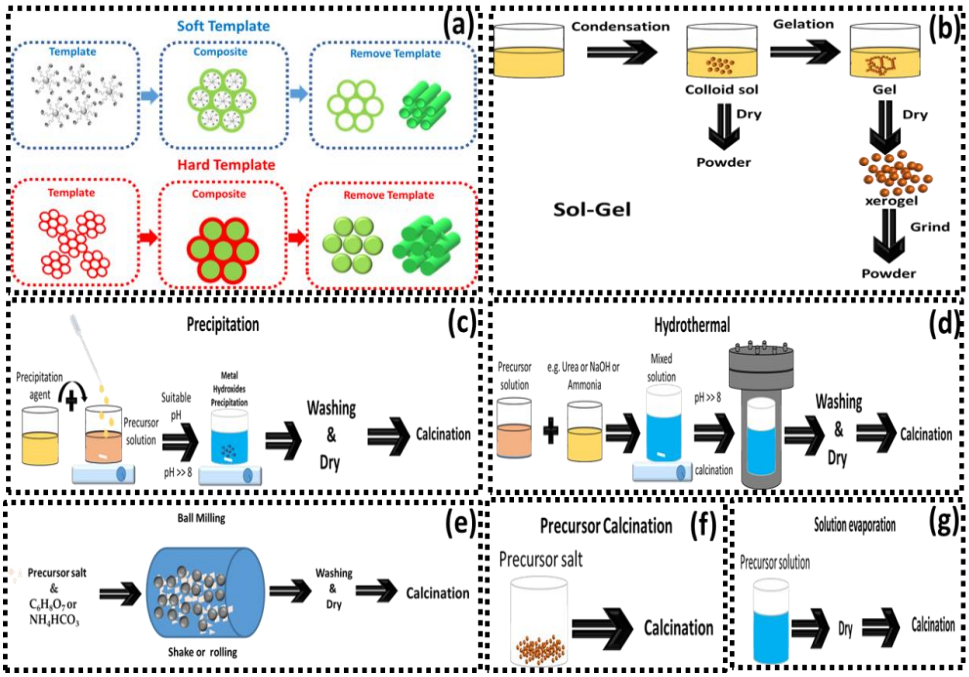

Scheme 2. Methods of synthesizing Co_3O_4: (**a**) templating, (**b**) sol–gel, (**c**) precipitation, (**d**) hydrothermal, (**e**) ball-milling, (**f**) precursor calcination, and (**g**) solution evaporation.

Fei et al. [92], Xu et al. [75], Hu et al. [93], Xu et al. [75], Fei et al. [92], Zhao et al. [94], Wang et al. [95], Zhou et al. [96], Wang et al. [70], Yang et al. [69], Bai et al. [68], Ma et al. [60], Ren et al. [73,97], Liu et al. [74], Liu et al. [98], and Li et al. [99] used a solvothermal–hydrothermal method at a reaction temperature of 80–180 °C to obtain Co_3O_4 catalysts with different morphologies. Typical patterns resulting from this method include cubes, nanorods, spheres, nanowires, nanotubes, microspheres, double-sided nanobrushes, 2D-nanoplates, 3D-nanoflowers, 1D-nanoneedles, 3D hierarchical cube-stacked microspheres, 3D hierarchical stacked needles, two-spheres with an urchin-like structure, 3D hierarchical fan-shaped stacked sheets, and dumbbell-brush-type. The specific surface area of these materials varied between 8 and 83 $m^2\ g^{-1}$. Additionally, Dissanayake et al. [21], Xie et al. [85], Mei et al. [100], Ren et al. [73], Liu et al. [58,71], Deng et al. [101], and Ma et al. [102] [89] synthesized three-dimensional (3D) or two-dimensional (2D) mesoporous Co_3O_4 materials using the template method with SBA-15, KIT-6, P123, and PMMA as templates. Except for PMMA, which was removed after calcination, the other templates were removed by washing with a highly concentrated solution of NaOH. The specific surface areas of the received Co_3O_4 catalysts were in the range of 21 to 553 $m^2\ g^{-1}$.

A sol–gel method was employed by Ercolino et al. [103], Puértolas et al. [104], Rivas et al. [33], Kirchnenova et al. [105], and Liu et al. [106] to synthesize Co_3O_4 catalysts. The final catalysts are calcined at a temperature of 350–600 °C, and the typical values of the specific surface area vary between 1 and 27 $m^2\ g^{-1}$. Several research groups, including Rivas et al. [33], Liu et al. [106], and Solsona et al. [107], have prepared Co_3O_4 catalysts through the application of a grinding technique that involves metal precursors and appropriate concentrations of $C_6H_8O_7$ or NH_4HCO_3. The resulting specific surface area ranged between 30 and 160 $m^2\ g^{-1}$ and was observed to be significantly dependent on the grinding time and the calcination temperature.

Recently, there has been a growing trend in synthesizing mesoporous catalysts through the thermal decomposition of MOFs (Liu et al. [72], Zhang et al. [108], Lie et al. [86], and Zhao et al. [109]). The shape of the final catalyst varies depending on the shape of the organic ligand

but is often in the form of void nanocages, octahedrons, and macroscopic hexagonal crystals. This synthesis method yields a specific surface area ranging from 2.5 to 118 $m^2\ g^{-1}$.

Figure 17 presents the percentage of Co_3O_4 catalysts prepared through various methods in relation to their specific surface area (S_{BET}). The majority of Co_3O_4 catalysts exhibited a specific surface area within the range 30–60 $m^2\ g^{-1}$, constituting 35% of the samples. Catalysts with a S_{BET} of 15–30 $m^2\ g^{-1}$ accounted for 25% of the samples. Finally, catalysts with specific surface areas in the low (<15 $m^2\ g^{-1}$) or high (>60 $m^2\ g^{-1}$) ranges represented around 20% of the samples, respectively.

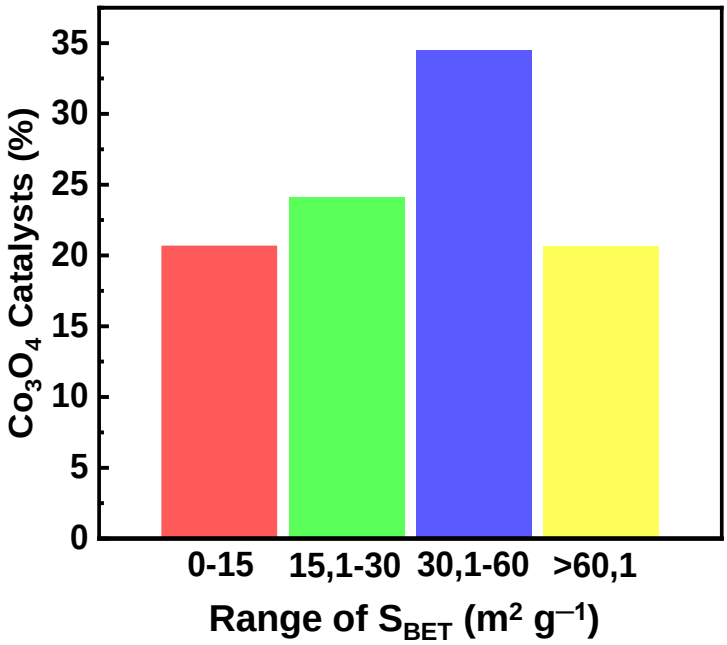

Figure 17. Percentage of reported Co_3O_4 (%) catalysts vs. range of S_{BET} ($m^2\ g^{-1}$).

5. Overall Conclusions, Challenges, and Perspectives

Catalytic oxidation is an effective after-treatment technology for the abatement of VOC emissions from industrial sources. The preparation of noble metal-free catalysts with high activity and stability remains challenging. This review focuses on Co_3O_4 catalysts, aiming at identifying the structure sensitivity of toluene oxidation as a case study. Particular attention has been paid to the specific reaction rate of the catalysts and its correlation with the textural and structural characteristics of Co_3O_4 samples. Extensive reference has been made to synthetic methods and characterization techniques to infer whether the catalytic performance is related to the specific surface area, morphology, facets, and surface oxidation state of the catalysts. From the aforementioned findings, it can be concluded that the specific surface area does not have a significant impact on the specific reaction rate of Co_3O_4 catalysts for the complete oxidation of toluene. However, the specific reaction rates differ due to factors such as the morphology, different exposed crystallographic planes, surface concentration, and oxidation state of cobalt cations. These factors are crucial in determining the specific reaction rate of Co_3O_4 by causing the formation of defects (steps, kinks, etc.) and oxygen vacancies or the development of oxygen species with different reactivities. More specifically, the preparation of Co_3O_4 with {110}, {220}, or {220}-{111} exposed crystallographic planes results in enhanced specific activity that could be attributed to the higher Co^{3+}/Co^{2+} surface ratio induced by the preferential exposure of Co^{3+} cations on the catalytic surface. On the other hand, when the only exposed plane is the {111} plane, which is populated by Co^{2+}, the catalytic surface is inactive for the oxidation of toluene. A high Co^{3+}/Co^{2+} ratio is a prerequisite for a high catalytic performance in the oxidation of VOCs.

In a broader context, the topic of the structure sensitivity of reactions taking place on catalytic surfaces has been raised mostly for supported noble metal catalysts. In the case

of metal oxide catalysts, structure sensitivity might theoretically manifest itself through two pathways as a function of the primary crystallite size of the oxide. The first pathway refers to the number density of surface defects and how this is influenced by the crystallite size and the specific surface area of the catalyst. It is typically expected that surface defects would lead to more active surface sites due to the presence of cations with a lower coordination number. Therefore, an increase in crystallite size (hence a decrease in the specific surface area) would lead to fewer defective crystals and, as a result, to a decrease in specific catalytic activity. However, such a behavior was not observed according to the analysis of this work since the specific activity of the catalysts did not show a definitive trend with variations in the specific surface area. The second pathway, which refers to the expression of different crystallographic planes (faceting) with a variation in crystallite size and the employed synthesis method, appears to be more relevant. Based on our analysis, the focus on developing Co_3O_4 catalysts with high specific surface areas does not suffice to prepare a highly active oxidation catalyst since the real challenge is to tailor the synthetic route to favor the development of surface traits that also contribute to the enhancement of the intrinsic activity of Co_3O_4 catalysts. Control of crystal orientation and shape can lead to the design of tailored nanomaterials with optimized catalytic function. The designated choice of a single oxide in the current review was a deliberate step taken to eliminate the influence of interactions among various phases or the support, which otherwise would complicate the analysis of catalytic performance metrics. This methodological approach is intended to ensure that the performance evaluation of the catalyst is based solely on its activity and not on any external factors that may interfere. It is noteworthy that the insights gained from this review can serve as a paradigm for other TMO-based catalysts that are commonly used in the field.

Author Contributions: Conceptualization, T.I.; methodology, T.I. and Y.G.; validation, M.S. and Y.G.; formal analysis, Y.G. and M.S.; data curation, M.S. and Y.G.; writing—original draft preparation, Y.G.; writing—review and editing, M.S. and T.I.; supervision, T.I.; project administration, T.I.; funding acquisition, T.I. All authors have read and agreed to the published version of the manuscript.

Funding: This research was funded by the Hellenic Foundation for Research and Innovation (H.F.R.I) under the "First Call for H.F.R.I Research Projects to support Faculty members and Researchers and the procurement of high-cost research equipment grant" (Project Number: HFRI-FM17-1876).

Conflicts of Interest: The authors declare no conflict of interest.

References

1. Ojala, S.; Koivikko, N.; Laitinen, T.; Mouammine, A.; Seelam, P.; Laassiri, S.; Ainassaari, K.; Brahmi, R.; Keiski, R. Utilization of Volatile Organic Compounds as an Alternative for Destructive Abatement. *Catalysts* **2015**, *5*, 1092–1151. [CrossRef]
2. Ciganek, M.; Neca, J. Chemical Characterization of Volatile Organic Compounds on Animal Farms. *Vet. Med.* **2008**, *53*, 641–651. [CrossRef]
3. Tai, X.H.; Lai, C.W.; Juan, J.C.; Lee, K.M. Nanocatalyst-Based Catalytic Oxidation Processes. In *Nanomaterials for Air Remediation*; Elsevier: Amsterdam, The Netherlands, 2020; pp. 133–150, ISBN 978-0-12-818821-7.
4. World Health Organization. Indoor Air Quality: Organic Pollutants. *EURO Rep. Stud.* **1989**, *111*, 1–70.
5. Anand, S.S.; Philip, B.K.; Mehendale, H.M. Volatile Organic Compounds. In *Encyclopedia of Toxicology*; Elsevier: Amsterdam, The Netherlands, 2014; pp. 967–970, ISBN 978-0-12-386455-0.
6. Bari, M.d.A.; Kindzierski, W.B.; Wheeler, A.J.; Héroux, M.-È.; Wallace, L.A. Source Apportionment of Indoor and Outdoor Volatile Organic Compounds at Homes in Edmonton, Canada. *Build. Environ.* **2015**, *90*, 114–124. [CrossRef]
7. Sax, S.N.; Bennett, D.H.; Chillrud, S.N.; Kinney, P.L.; Spengler, J.D. Differences in Source Emission Rates of Volatile Organic Compounds in Inner-City Residences of New York City and Los Angeles. *J. Expo. Sci. Env. Epidemiol.* **2004**, *14*, S95–S109. [CrossRef] [PubMed]
8. Son, B.; Breysse, P.; Yang, W. Volatile Organic Compounds Concentrations in Residential Indoor and Outdoor and Its Personal Exposure in Korea. *Environ. Int.* **2003**, *29*, 79–85. [CrossRef] [PubMed]
9. Brown, S.K.; Sim, M.R.; Abramson, M.J.; Gray, C.N. Concentrations of Volatile Organic Compounds in Indoor Air—A Review. *Indoor Air* **1994**, *4*, 123–134. [CrossRef]
10. National Institutes of Health; National Institute of Environmental Health Sciences. *Environmental Health Perspectives: Supplements*; U.S. Department of Health and Human Services, Public Health Service, National Institutes of Health, National Institute of Environmental Health Sciences: Research Triangle Park, NV, USA, 1993.

11. Lewandowski, D.A. *Design of Thermal Oxidation Systems for Volatile Organic Compounds*; CRC Press: Boca Raton, FL, USA, 1999; ISBN 1-56670-410-3.
12. Deshmukh, S.; Vlachos, D. A Reduced Mechanism for Methane and One-Step Rate Expressions for Fuel-Lean Catalytic Combustion of Small Alkanes on Noble Metals. *Combust. Flame* **2007**, *149*, 366–383. [CrossRef]
13. Badra, J.A.; Masri, A.R. Catalytic Combustion of Selected Hydrocarbon Fuels on Platinum: Reactivity and Hetero–Homogeneous Interactions. *Combust. Flame* **2012**, *159*, 817–831. [CrossRef]
14. Fierro, J.L.G. *Metal Oxides: Chemistry and Applications*; Taylor & Francis: Boca Raton, FL, USA, 2006; ISBN 978-1-4200-2812-6.
15. Liotta, L.F. Catalytic Oxidation of Volatile Organic Compounds on Supported Noble Metals. *Appl. Catal. B Environ.* **2010**, *100*, 403–412. [CrossRef]
16. Aznárez, A.; Gil, A.; Korili, S.A. Performance of Palladium and Platinum Supported on Alumina Pillared Clays in the Catalytic Combustion of Propene. *RSC Adv.* **2015**, *5*, 82296–82309. [CrossRef]
17. Saqer, S.M.; Kondarides, D.I.; Verykios, X.E. Catalytic Oxidation of Toluene over Binary Mixtures of Copper, Manganese and Cerium Oxides Supported on γ-Al_2O_3. *Appl. Catal. B Environ.* **2011**, *103*, 275–286. [CrossRef]
18. Wang, C.-H. Al_2O_3-Supported Transition-Metal Oxide Catalysts for Catalytic Incineration of Toluene. *Chemosphere* **2004**, *55*, 11–17. [CrossRef] [PubMed]
19. Azalim, S.; Franco, M.; Brahmi, R.; Giraudon, J.-M.; Lamonier, J.-F. Removal of Oxygenated Volatile Organic Compounds by Catalytic Oxidation over Zr–Ce–Mn Catalysts. *J. Hazard. Mater.* **2011**, *188*, 422–427. [CrossRef] [PubMed]
20. Lany, S. Semiconducting Transition Metal Oxides. *J. Phys. Condens. Matter* **2015**, *27*, 283203. [CrossRef] [PubMed]
21. Dissanayake, S.; Wasalathanthri, N.; Shirazi Amin, A.; He, J.; Poges, S.; Rathnayake, D.; Suib, S.L. Mesoporous Co_3O_4 Catalysts for VOC Elimination: Oxidation of 2-Propanol. *Appl. Catal. A Gen.* **2020**, *590*, 117366. [CrossRef]
22. Li, G.; Zhang, C.; Wang, Z.; Huang, H.; Peng, H.; Li, X. Fabrication of Mesoporous Co_3O_4 Oxides by Acid Treatment and Their Catalytic Performances for Toluene Oxidation. *Appl. Catal. A Gen.* **2018**, *550*, 67–76. [CrossRef]
23. González-Prior, J.; López-Fonseca, R.; Gutiérrez-Ortiz, J.I.; de Rivas, B. Oxidation of 1,2-Dichloroethane over Nanocube-Shaped Co_3O_4 Catalysts. *Appl. Catal. B Environ.* **2016**, *199*, 384–393. [CrossRef]
24. De Rivas, B.; López-Fonseca, R.; Jiménez-González, C.; Gutiérrez-Ortiz, J.I. Highly Active Behaviour of Nanocrystalline Co_3O_4 from Oxalate Nanorods in the Oxidation of Chlorinated Short Chain Alkanes. *Chem. Eng. J.* **2012**, *184*, 184–192. [CrossRef]
25. Zhao, Q.; Shih, W.Y.; Shih, W.-H. Effects of Processing Parameters on the Morphology of Precipitated Manganese Oxide Powders. *Ind. Eng. Chem. Res.* **2009**, *48*, 1490–1494. [CrossRef]
26. Yang, X.; Yu, X.; Lin, M.; Ma, X.; Ge, M. Enhancement Effect of Acid Treatment on Mn_2O_3 Catalyst for Toluene Oxidation. *Catal. Today* **2019**, *327*, 254–261. [CrossRef]
27. Deng, J.; He, S.; Xie, S.; Yang, H.; Liu, Y.; Guo, G.; Dai, H. Ultralow Loading of Silver Nanoparticles on Mn_2O_3 Nanowires Derived with Molten Salts: A High-Efficiency Catalyst for the Oxidative Removal of Toluene. *Environ. Sci. Technol.* **2015**, *49*, 11089–11095. [CrossRef] [PubMed]
28. Scirè, S.; Minicò, S.; Crisafulli, C.; Galvagno, S. Catalytic Combustion of Volatile Organic Compounds over Group IB Metal Catalysts on Fe_2O_3. *Catal. Commun.* **2001**, *2*, 229–232. [CrossRef]
29. Gu, Z.; Hohn, K.L. Catalytic Oxidation of Methanol on Nanoscale Copper Oxide and Nickel Oxide. *Ind. Eng. Chem. Res.* **2004**, *43*, 30–35. [CrossRef]
30. Morales, M.; Barbero, B.; Cadus, L. Total Oxidation of Ethanol and Propane over Mn-Cu Mixed Oxide Catalysts. *Appl. Catal. B Environ.* **2006**, *67*, 229–236. [CrossRef]
31. Delimaris, D.; Ioannides, T. VOC Oxidation over CuO–CeO_2 Catalysts Prepared by a Combustion Method. *Appl. Catal. B Environ.* **2009**, *89*, 295–302. [CrossRef]
32. Yan, Q.; Li, X.; Zhao, Q.; Chen, G. Shape-Controlled Fabrication of the Porous Co_3O_4 Nanoflower Clusters for Efficient Catalytic Oxidation of Gaseous Toluene. *J. Hazard. Mater.* **2012**, *209–210*, 385–391. [CrossRef]
33. De Rivas, B.; López-Fonseca, R.; Jiménez-González, C.; Gutiérrez-Ortiz, J.I. Synthesis, Characterisation and Catalytic Performance of Nanocrystalline Co_3O_4 for Gas-Phase Chlorinated VOC Abatement. *J. Catal.* **2011**, *281*, 88–97. [CrossRef]
34. Smyrnioti, M.; Ioannides, T. Synthesis of Cobalt-Based Nanomaterials from Organic Precursors. In *Cobalt*; Maaz, K., Ed.; InTech: Rijeka, Croatia, 2017; ISBN 978-953-51-3667-5.
35. Kong, F.-C.; Li, Y.-F.; Shang, C.; Liu, Z.-P. Stability and Phase Transition of Cobalt Oxide Phases by Machine Learning Global Potential Energy Surface. *J. Phys. Chem. C* **2019**, *123*, 17539–17547. [CrossRef]
36. Qiao, L.; Xiao, H.Y.; Meyer, H.M.; Sun, J.N.; Rouleau, C.M.; Puretzky, A.A.; Geohegan, D.B.; Ivanov, I.N.; Yoon, M.; Weber, W.J.; et al. Nature of the Band Gap and Origin of the Electro-/Photo-Activity of Co_3O_4. *J. Mater. Chem. C* **2013**, *1*, 4628. [CrossRef]
37. Zhong, J.; Zeng, Y.; Zhang, M.; Feng, W.; Xiao, D.; Wu, J.; Chen, P.; Fu, M.; Ye, D. Toluene Oxidation Process and Proper Mechanism over Co_3O_4 Nanotubes: Investigation through In-Situ DRIFTS Combined with PTR-TOF-MS and Quasi in-Situ XPS. *Chem. Eng. J.* **2020**, *397*, 125375. [CrossRef]
38. Ren, Q.; Zhao, X.; Zhong, J.; Zhang, J.; Tian, J.; Yan, D.; Liu, P.; Fu, M.; Chen, L.; Wu, J.; et al. Unravelling the Role of Oxygen Species in Toluene Oxidation over Co_3O_4-Base Catalysts: In Situ DRIFTS Coupled with Quasi in Situ XPS. *J. Catal.* **2023**, *418*, 130–140. [CrossRef]
39. Doornkamp, C.; Ponec, V. The Universal Character of the Mars and Van Krevelen Mechanism. *J. Mol. Catal. A Chem.* **2000**, *162*, 19–32. [CrossRef]

40. Vannice, M.A. An Analysis of the Mars–van Krevelen Rate Expression. *Catal. Today* **2007**, *123*, 18–22. [CrossRef]
41. Carrero, C.A.; Schloegl, R.; Wachs, I.E.; Schomaecker, R. Critical Literature Review of the Kinetics for the Oxidative Dehydrogenation of Propane over Well-Defined Supported Vanadium Oxide Catalysts. *ACS Catal.* **2014**, *4*, 3357–3380. [CrossRef]
42. Xie, X.; Shen, W. Morphology Control of Cobalt Oxide Nanocrystals for Promoting Their Catalytic Performance. *Nanoscale* **2009**, *1*, 50. [CrossRef]
43. Barteau, M.A.; Vohs, J.M. Structure Sensitivity of Reactions on Metal Oxide Surfaces. In *Studies in Surface Science and Catalysis*; Elsevier: Amsterdam, The Netherlands, 1989; Volume 44, pp. 89–95, ISBN 978-0-444-87146-6.
44. Boudart, M. Catalysis by Supported Metals. In *Advances in Catalysis*; Elsevier: Amsterdam, The Netherlands, 1969; Volume 20, pp. 153–166, ISBN 978-0-12-007820-2.
45. Zafiris, G.S.; Gorte, R.J. CO Oxidation on Pt/α-Al_2O_3(0001): Evidence for Structure Sensitivity. *J. Catal.* **1993**, *140*, 418–423. [CrossRef]
46. Hicks, R.; Qi, H.; Young, M.L.; Lee, R.G. Structure Sensitivity of Methane Oxidation over Platinum and Palladium. *J. Catal.* **1990**, *122*, 280–294. [CrossRef]
47. Yokota, S.; Okumura, K.; Niwa, M. Support Effect of Metal Oxide on Rh Catalysts in the CH_4-CO_2 Reforming Reaction. *Catal. Lett.* **2002**, *84*, 131–134. [CrossRef]
48. Haruta, M. Novel Catalysis of Gold Deposited on Metal Oxides. *Catal. Surv. Jpn.* **1997**, *1*, 61–73. [CrossRef]
49. Volta, J.C.; Portefaix, J.L. Structure Sensitivity of Mild Oxidation Reactions on Oxide Catalysts—A Review. *Appl. Catal.* **1985**, *18*, 1–32. [CrossRef]
50. Ginés, M.J.L.; Amadeo, N.; Laborde, M.; Apesteguía, C.R. Activity and Structure-Sensitivity of the Water-Gas Shift Reaction over CuZnAl Mixed Oxide Catalysts. *Appl. Catal. A Gen.* **1995**, *131*, 283–296. [CrossRef]
51. Tatibouet, J.; Phichitkul, C.; Germain, J.E. Structure-Sensitive Catalytic Oxidation of Butenes on Molybdenum Trioxide Crystallites. *J. Catal.* **1986**, *99*, 231–234. [CrossRef]
52. Natile, M.M.; Glisenti, A. Study of Surface Reactivity of Cobalt Oxides: Interaction with Methanol. *Chem. Mater.* **2002**, *14*, 3090–3099. [CrossRef]
53. Zhou, K.; Liu, J.; Wen, P.; Hu, Y.; Gui, Z. Morphology-Controlled Synthesis of Co_3O_4 by One Step Template-Free Hydrothermal Method. *Mater. Res. Bull.* **2015**, *67*, 87–93. [CrossRef]
54. Hosseini, S.; Niaei, A.; Salari, D. Preparation and Characterization of Nano- and Non-Nanoscale Co_3O_4 Spinels Obtained from Different Methods and Study of Their Performance in Combustion of Aromatics from Polluted Air-A Comparison with Pt/γ-Al_2O_3 Performance. *J. Environ. Sci. Health Part A* **2012**, *47*, 1728–1732. [CrossRef] [PubMed]
55. Wang, X.; Chen, X.; Gao, L.; Zheng, H.; Zhang, Z.; Qian, Y. One-Dimensional Arrays of Co_3O_4 Nanoparticles: Synthesis, Characterization, and Optical and Electrochemical Properties. *J. Phys. Chem. B* **2004**, *108*, 16401–16404. [CrossRef]
56. Zhou, H.; Lv, B.; Wu, D.; Xu, Y. Synthesis of Polycrystalline Co_3O_4 Nanowires with Excellent Ammonium Perchlorate Catalytic Decomposition Property. *Mater. Res. Bull.* **2014**, *60*, 492–497. [CrossRef]
57. He, T.; Chen, D.; Jiao, X.; Wang, Y. Co_3O_4 Nanoboxes: Surfactant-Templated Fabrication and Microstructure Characterization. *Adv. Mater.* **2006**, *18*, 1078–1082. [CrossRef]
58. Liu, Y.; Dai, H.; Deng, J.; Zhang, L.; Zhao, Z.; Li, X.; Wang, Y.; Xie, S.; Yang, H.; Guo, G. Controlled Generation of Uniform Spherical $LaMnO_3$, $LaCoO_3$, Mn_2O_3, and Co_3O_4 Nanoparticles and Their High Catalytic Performance for Carbon Monoxide and Toluene Oxidation. *Inorg. Chem.* **2013**, *52*, 8665–8676. [CrossRef]
59. Nguyen, H.; El-Safty, S.A. Meso- and Macroporous Co_3O_4 Nanorods for Effective VOC Gas Sensors. *J. Phys. Chem. C* **2011**, *115*, 8466–8474. [CrossRef]
60. Ma, X.; Yu, X.; Yang, X.; Lin, M.; Ge, M. Hydrothermal Synthesis of a Novel Double-sided Nanobrush Co_3O_4 Catalyst and Its Catalytic Performance for Benzene Oxidation. *ChemCatChem* **2018**, *11*, cctc.201801539. [CrossRef]
61. Deng, S.; Liu, X.; Chen, N.; Deng, D.; Xiao, X.; Wang, Y. A Highly Sensitive VOC Gas Sensor Using P-Type Mesoporous Co_3O_4 Nanosheets Prepared by a Facile Chemical Coprecipitation Method. *Sens. Actuators B Chem.* **2016**, *233*, 615–623. [CrossRef]
62. Li, W.Y.; Xu, L.N.; Chen, J. Co_3O_4 Nanomaterials in Lithium-Ion Batteries and Gas Sensors. *Adv. Funct. Mater.* **2005**, *15*, 851–857. [CrossRef]
63. Dong, J.; Song, L.; Yin, J.-J.; He, W.; Wu, Y.; Gu, N.; Zhang, Y. Co_3O_4 Nanoparticles with Multi-Enzyme Activities and Their Application in Immunohistochemical Assay. *ACS Appl. Mater. Interfaces* **2014**, *6*, 1959–1970. [CrossRef] [PubMed]
64. Liotta, L.F.; Wu, H.; Pantaleo, G.; Venezia, A.M. Co_3O_4 Nanocrystals and Co_3O_4–MO_x Binary Oxides for CO, CH_4 and VOC Oxidation at Low Temperatures: A Review. *Catal. Sci. Technol.* **2013**, *3*, 3085. [CrossRef]
65. Kamal, M.S.; Razzak, S.A.; Hossain, M.M. Catalytic Oxidation of Volatile Organic Compounds (VOCs)—A Review. *Atmos. Environ.* **2016**, *140*, 117–134. [CrossRef]
66. Hosseini, S.A. Catalytic Oxidation of Volatile Organic Compounds by Using Spinel Mixed Oxide Catalyst—A Review. *Adv. Ceram. Sci. Eng.* **2016**, *5*, 117–134. [CrossRef]
67. Tang, W.; Liu, G.; Li, D.; Liu, H.; Wu, X.; Han, N.; Chen, Y. Design and Synthesis of Porous Non-Noble Metal Oxides for Catalytic Removal of VOCs. *Sci. China Chem.* **2015**, *58*, 1359–1366. [CrossRef]
68. Bai, G.; Dai, H.; Deng, J.; Liu, Y.; Wang, F.; Zhao, Z.; Qiu, W.; Au, C.T. Porous Co_3O_4 Nanowires and Nanorods: Highly Active Catalysts for the Combustion of Toluene. *Appl. Catal. A Gen.* **2013**, *450*, 42–49. [CrossRef]

69. Yang, H.; Dai, H.; Deng, J.; Xie, S.; Han, W.; Tan, W.; Jiang, Y.; Au, C.T. Porous Cube-Aggregated Co_3O_4 Microsphere-Supported Gold Nanoparticles for Oxidation of Carbon Monoxide and Toluene. *ChemSusChem* **2014**, *7*, 1745–1754. [CrossRef] [PubMed]
70. Wang, F.; Dai, H.; Deng, J.; Xie, S.; Yang, H.; Han, W. Nanoplate-Aggregate Co_3O_4 Microspheres for Toluene Combustion. *Chin. J. Catal.* **2014**, *35*, 1475–1481. [CrossRef]
71. Liu, Y.; Dai, H.; Deng, J.; Xie, S.; Yang, H.; Tan, W.; Han, W.; Jiang, Y.; Guo, G. Mesoporous Co_3O_4-Supported Gold Nanocatalysts: Highly Active for the Oxidation of Carbon Monoxide, Benzene, Toluene, and o-Xylene. *J. Catal.* **2014**, *309*, 408–418. [CrossRef]
72. Liu, X.; Wang, J.; Zeng, J.; Wang, X.; Zhu, T. Catalytic Oxidation of Toluene over a Porous Co_3O_4-Supported Ruthenium Catalyst. *RSC Adv.* **2015**, *5*, 52066–52071. [CrossRef]
73. Ren, Q.; Mo, S.; Peng, R.; Feng, Z.; Zhang, M.; Chen, L.; Fu, M.; Wu, J.; Ye, D. Controllable Synthesis of 3D Hierarchical Co_3O_4 Nanocatalysts with Various Morphologies for the Catalytic Oxidation of Toluene. *J. Mater. Chem. A* **2018**, *6*, 498–509. [CrossRef]
74. Liu, W.; Liu, R.; Zhang, X. Controllable Synthesis of 3D Hierarchical Co_3O_4 Catalysts and Their Excellent Catalytic Performance for Toluene Combustion. *Appl. Surf. Sci.* **2020**, *507*, 145174. [CrossRef]
75. Xu, W.; Xiao, K.; Lai, S.; Liang, J.; Jiang, X.; Liu, Z.; Li, F.; Zhang, Y.; Wu, X.; Zhou, X. Designing a Dumbbell-Brush-Type Co_3O_4 for Efficient Catalytic Toluene Oxidation. *Catal. Commun.* **2020**, *140*, 106005. [CrossRef]
76. Scherrer, P. Estimation of the Size and Internal Structure of Colloidal Particles by Means of Röntgen. *Nachr. Ges. Wiss. Göttingen* **1918**, *2*, 96–100.
77. Raveau, B.; Seikh, M. Crystal Chemistry of Cobalt Oxides. In *Cobalt Oxides*; Wiley-VCH Verlag GmbH & Co. KGaA: Weinheim, Germany, 2012; pp. 3–70, ISBN 978-3-527-64552-7.
78. Casas-Cabanas, M.; Binotto, G.; Larcher, D.; Lecup, A.; Giordani, V.; Tarascon, J.-M. Defect Chemistry and Catalytic Activity of Nanosized Co_3O_4. *Chem. Mater.* **2009**, *21*, 1939–1947. [CrossRef]
79. Zhang, W.; Wu, F.; Li, J.; You, Z. Dispersion–Precipitation Synthesis of Highly Active Nanosized Co_3O_4 for Catalytic Oxidation of Carbon Monoxide and Propane. *Appl. Surf. Sci.* **2017**, *411*, 136–143. [CrossRef]
80. Chuang, T.J.; Brundle, C.R.; Rice, D.W. Interpretation of the X-Ray Photoemission Spectra of Cobalt Oxides and Cobalt Oxide Surfaces. *Surf. Sci.* **1976**, *59*, 413–429. [CrossRef]
81. Jiménez, V.M.; Fernández, A.; Espinós, J.P.; González-Elipe, A.R. The State of the Oxygen at the Surface of Polycrystalline Cobalt Oxide. *J. Electron. Spectrosc. Relat. Phenom.* **1995**, *71*, 61–71. [CrossRef]
82. Diallo, A.; Beye, A.C.; Doyle, T.B.; Park, E.; Maaza, M. Green Synthesis of Co_3O_4 Nanoparticles via *Aspalathus linearis*: Physical Properties. *Green. Chem. Lett. Rev.* **2015**, *8*, 30–36. [CrossRef]
83. Lei, J.; Wang, S.; Li, J. Mesoporous Co_3O_4 Derived from Co-MOFs with Different Morphologies and Ligands for Toluene Catalytic Oxidation. *Chem. Eng. Sci.* **2020**, *220*, 115654. [CrossRef]
84. Davies, T.E.; García, T.; Solsona, B.; Taylor, S.H. Nanocrystalline Cobalt Oxide: A Catalyst for Selective Alkane Oxidation under Ambient Conditions. *Chem. Commun.* **2006**, *32*, 3417–3419. [CrossRef] [PubMed]
85. Xie, H.; Lan, H.; Tan, X.; Wang, W.; Yan, L.; Liu, X.; Zhou, G. High-Efficient Oxidation Removal of Ethanol from Air over Ordered Mesoporous Co_3O_4/KIT-6 Catalyst. *J. Environ. Chem. Eng.* **2019**, *7*, 103480. [CrossRef]
86. Lei, J.; Wang, S.; Li, J. Mesoporous Co_3O_4 Derived from Facile Calcination of Octahedral Co-MOFs for Toluene Catalytic Oxidation. *Ind. Eng. Chem. Res.* **2020**, *59*, 5583–5590. [CrossRef]
87. Ren, Z.; Wu, Z.; Song, W.; Xiao, W.; Guo, Y.; Ding, J.; Suib, S.L.; Gao, P.-X. Low Temperature Propane Oxidation over Co_3O_4 Based Nano-Array Catalysts: Ni Dopant Effect, Reaction Mechanism and Structural Stability. *Appl. Catal. B Environ.* **2016**, *180*, 150–160. [CrossRef]
88. Liotta, L.F.; Di Carlo, G.; Pantaleo, G.; Deganello, G. Catalytic Performance of Co_3O_4/CeO_2 and Co_3O_4/CeO_2–ZrO_2 Composite Oxides for Methane Combustion: Influence of Catalyst Pretreatment Temperature and Oxygen Concentration in the Reaction Mixture. *Appl. Catal. B Environ.* **2007**, *70*, 314–322. [CrossRef]
89. Ma, C.Y.; Mu, Z.; Li, J.J.; Jin, Y.G.; Cheng, J.; Lu, G.Q.; Hao, Z.P.; Qiao, S.Z. Mesoporous Co_3O_4 and Au/Co_3O_4 Catalysts for Low-Temperature Oxidation of Trace Ethylene. *J. Am. Chem. Soc.* **2010**, *132*, 2608–2613. [CrossRef]
90. Fan, Z.; Zhang, Z.; Fang, W.; Yao, X.; Zou, G.; Shangguan, W. Low-Temperature Catalytic Oxidation of Formaldehyde over Co_3O_4 Catalysts Prepared Using Various Precipitants. *Chin. J. Catal.* **2016**, *37*, 947–954. [CrossRef]
91. Anke, S.; Bendt, G.; Sinev, I.; Hajiyani, H.; Antoni, H.; Zegkinoglou, I.; Jeon, H.; Pentcheva, R.; Roldan Cuenya, B.; Schulz, S.; et al. Selective 2-Propanol Oxidation over Unsupported Co_3O_4 Spinel Nanoparticles: Mechanistic Insights into Aerobic Oxidation of Alcohols. *ACS Catal.* **2019**, *9*, 5974–5985. [CrossRef]
92. Fei, X.; Cao, S.; Ouyang, W.; Wen, Y.; Wang, H.; Wu, Z. A Convenient Synthesis of Core-Shell Co_3O_4@ZSM-5 Catalysts for the Total Oxidation of Dichloromethane (CH_2Cl_2). *Chem. Eng. J.* **2020**, *387*, 123411. [CrossRef]
93. Hu, L.; Peng, Q.; Li, Y. Selective Synthesis of Co_3O_4 Nanocrystal with Different Shape and Crystal Plane Effect on Catalytic Property for Methane Combustion. *J. Am. Chem. Soc.* **2008**, *130*, 16136–16137. [CrossRef] [PubMed]
94. Zhao, Q.; Liu, Q.; Zheng, Y.; Han, R.; Song, C.; Ji, N.; Ma, D. Enhanced Catalytic Performance for Volatile Organic Compound Oxidation over In-Situ Growth of MnO_x on Co_3O_4 Nanowire. *Chemosphere* **2020**, *244*, 125532. [CrossRef] [PubMed]
95. Wang, C.; Hua, W.; Chai, G.; Zhang, C.; Guo, Y. Insights into the Morphological Effect of Co_3O_4 Crystallite on Catalytic Oxidation of Vinyl Chloride. *Catalysts* **2019**, *9*, 408. [CrossRef]
96. Zhou, M.; Zhang, J.; Liao, L.; Wu, W. Enhanced Catalytic Methane Combustion over Co_3O_4 Nanowire Arrays by Cation Substitution. *Mater. Res. Express* **2017**, *4*, 125006. [CrossRef]

97. Ren, Q.; Feng, Z.; Mo, S.; Huang, C.; Li, S.; Zhang, W.; Chen, L.; Fu, M.; Wu, J.; Ye, D. 1D-Co_3O_4, 2D-Co_3O_4, 3D-Co_3O_4 for Catalytic Oxidation of Toluene. *Catal. Today* **2019**, *332*, 160–167. [CrossRef]
98. Liu, S.; Liu, P.; Niu, R.; Wang, S.; Li, J. Facile Synthesis of Mesoporous Co_3O_4 Nanoflowers for Catalytic Combustion of Ventilation Air Methane. *Chem. Res. Chin. Univ.* **2017**, *33*, 965–970. [CrossRef]
99. Li, K.; Chen, J.; Bai, B.; Zhao, S.; Hu, F.; Li, J. Bridging the Reaction Route of Toluene Total Oxidation and the Structure of Ordered Mesoporous Co_3O_4: The Roles of Surface Sodium and Adsorbed Oxygen. *Catal. Today* **2017**, *297*, 173–181. [CrossRef]
100. Mei, J.; Xie, J.; Qu, Z.; Ke, Y.; Hu, X.; Yan, N. Ordered Mesoporous Spinel Co_3O_4 as a Promising Catalyst for the Catalytic Oxidation of Dibromomethane. *Mol. Catal.* **2018**, *461*, 60–66. [CrossRef]
101. Deng, J.; Zhang, L.; Dai, H.; Xia, Y.; Jiang, H.; Zhang, H.; He, H. Ultrasound-Assisted Nanocasting Fabrication of Ordered Mesoporous MnO_2 and Co_3O_4 with High Surface Areas and Polycrystalline Walls. *J. Phys. Chem. C* **2010**, *114*, 2694–2700. [CrossRef]
102. Ma, C.; Mu, Z.; He, C.; Li, P.; Li, J.; Hao, Z. Catalytic Oxidation of Benzene over Nanostructured Porous Co_3O_4-CeO_2 Composite Catalysts. *J. Environ. Sci.* **2011**, *23*, 2078–2086. [CrossRef] [PubMed]
103. Ercolino, G.; Stelmachowski, P.; Grzybek, G.; Kotarba, A.; Specchia, S. Optimization of Pd Catalysts Supported on Co_3O_4 for Low-Temperature Lean Combustion of Residual Methane. *Appl. Catal. B Environ.* **2017**, *206*, 712–725. [CrossRef]
104. Puértolas, B.; Smith, A.; Vázquez, I.; Dejoz, A.; Moragues, A.; Garcia, T.; Solsona, B. The Different Catalytic Behaviour in the Propane Total Oxidation of Cobalt and Manganese Oxides Prepared by a Wet Combustion Procedure. *Chem. Eng. J.* **2013**, *229*, 547–558. [CrossRef]
105. Kirchnerova, J.; Alifanti, M.; Delmon, B. Evidence of Phase Cooperation in the $LaCoO_3$–CeO_2–Co_3O_4 Catalytic System in Relation to Activity in Methane Combustion. *Appl. Catal. A Gen.* **2002**, *231*, 65–80. [CrossRef]
106. Liu, Q.; Wang, L.-C.; Chen, M.; Cao, Y.; He, H.-Y.; Fan, K.-N. Dry Citrate-Precursor Synthesized Nanocrystalline Cobalt Oxide as Highly Active Catalyst for Total Oxidation of Propane. *J. Catal.* **2009**, *263*, 104–113. [CrossRef]
107. Solsona, B.; Vázquez, I.; Garcia, T.; Davies, T.E.; Taylor, S.H. Complete Oxidation of Short Chain Alkanes Using a Nanocrystalline Cobalt Oxide Catalyst. *Catal. Lett.* **2007**, *116*, 116–121. [CrossRef]
108. Zhang, M.; Zou, S.; Zhang, Q.; Mo, S.; Zhong, J.; Chen, D.; Fu, M.; Chen, P.; Ye, D. Macroscopic Hexagonal Co_3 O_4 Tubes Derived from Controllable Two-Dimensional Metal-Organic Layer Single Crystals: Formation Mechanism and Catalytic Activity. *Inorg. Chem.* **2020**, *59*, 3062–3071. [CrossRef]
109. Zhao, J.; Tang, Z.; Dong, F.; Zhang, J. Controlled Porous Hollow Co_3O_4 Polyhedral Nanocages Derived from Metal-Organic Frameworks (MOFs) for Toluene Catalytic Oxidation. *Mol. Catal.* **2019**, *463*, 77–86. [CrossRef]